university of groningen

faculty of science and engineering

MASTER THESIS

Development of an experimental setup to study droplet dynamics at micro- and millimeter scale

Fleur Veen

Supervisor and first examiner:
Prof. Dr. Ir. R. Hoekstra
Second examiner:
Prof. Dr. O. O. Versolato

University of Groningen
May 2025

Abstract

The deformation of droplets after laser impact has recently gained more interest because of its application in EUV nanolithography machines. In the source of these machines, a laser pulse is fired at liquid tin droplets to deform the droplet into a suitable target for plasma generation. The droplet deformation process is studied extensively, by using a combination of shadowgraphy and stroboscopic imaging techniques. However, the high refractive index of tin does not allow for the visualization of pressure fields inside the droplet, something a transparent medium like water does allow for. Due to dynamic similarity in fluid flows, the droplet deformation of water can be compared to tin if non-dimensional parameters like the Weber number are the same. This thesis describes the development of two experimental setups, which can be used to visualize droplet deformation at the micro- and millimeter length scale. First an experimental setup at millimeter scale is designed, to evaluate methods for studying water droplet deformation, where water droplets are deformed by impact on a similar sized pillar. The setup is characterized in terms of droplet size and droplet velocity, giving a Weber number range of 50 – 550. Then a setup at micrometer scale is designed, where microdroplets are generated using a piezo-actuated droplet-on-demand system, operated in negative pulse voltage mode. Characterization results show the system can produce droplets in a diameter range of d = 83 – 100 μm, with velocities of v_d = 0.9 – 2.2 m/s, depending on the liquid properties and generator settings. Due to the low Weber number of droplet impact on a pillar, its radial expansion is limited, resulting in oscillation of the droplet. In an outlook, a vacuum setup is briefly introduced, which can allow for future studies of droplet deformation at micrometer scale in a low pressure environment.

Contents

Chapter 1

Introduction

Modern nanolithography machines use extreme ultra violet (EUV) light of 13.5 nm in the manufacturing process of microchips. For the generation of EUV light, two laser pulses are fired at a tin liquid droplet stream: a pre-pulse and a main-pulse. The pre-pulse ($\sim$ 10 ns) is used for shaping tin droplets into a thin sheet, which is a suitable target for the main pulse. After impact on the droplet surface, the pre-pulse generates a plasma front at the laser facing side of the droplet surface. The localized plasma formation induces a pressure kick on the droplet, which subsequently deforms and accelerates the droplet. In a timescale of a few nanoseconds the droplet is accelerated to a center of mass propulsion velocity in the order of 100 m/s. Due to this acceleration, the droplet diameter expands in the radial direction. From its initial spherical shape, the droplet deforms into a sheet of with a diameter of 500 µm. After formation of this sheet, the main pulse is used to create an EUV emitting tin plasma.

The formation of an optimal target requires control over the droplet's deformation and propulsion velocity. This requires fundamental knowledge about the fluid dynamic response of the droplet after laser impact. Extensive research of sheet formation and eventual sheet fragmentation has already been done [2, 3]. The visualization of pressure waves inside tin droplets after laser impact, can provide more insights to fundamentally understand the fluid dynamic processes. Visualization of pressure changes in fluid flows can be achieved by employing the Schlieren imaging technique. This imaging technique relies on changes in refractive index of light that travels through a fluid flow [4]. Utilization of the

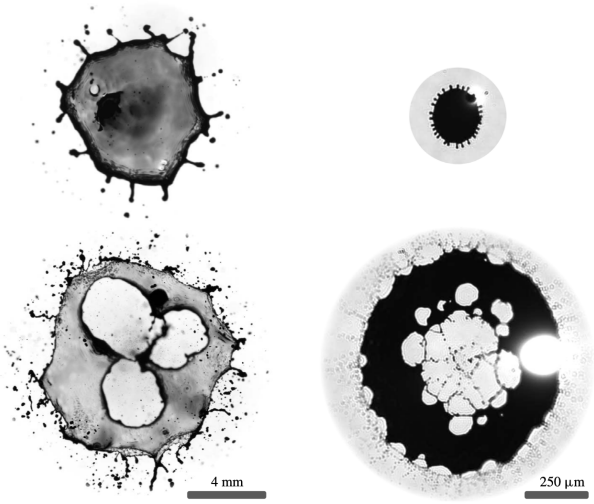

Figure 1.1: An example of the concept of dynamic similarity in fluid flows. Left side images show the sheet formation and fragmentation of methyl-ethyl-ketone (MEK) droplets. On the right hand side, images of the plasma-induced sheet formation and fragmentation of micrometer sized tin droplets are shown. Taken with permission from [1]

Schlieren imaging technique requires a transparent medium, motivating the research of laser-droplet interaction with transparent liquids.

The concept of dynamic similarity, a common concept in fluid dynamics, will be used to compare fluid dynamics of different liquids. Dynamic similarity allows for the comparison of different fluid flows, if the non-dimensional parameters that govern fluid motion are the same. After laser impact, where the ratio between surface tension and inertia forces determines the droplet deformation, the associated Weber number can be used to categorize fluid characteristics. This concept has already been applied, when comparing the deformation and fragmentation of vapor propelled millimeter sized methyl-ethyl-ketone (MEK) droplets to plasma-induced deformation of micrometer sized tin droplets [5]. Images illustrating the similarity in sheet formation and sheet fragmentation of MEK and tin droplets are shown in Figure 1.1. However, at this length scale the laser beam profile has been shown to influence features of sheet fragmentation [6]. Therefore, an experimental setup at the micrometer scale, for laser-droplet impact of transparent liquids, will be realized instead.

The focus of this research project is the development of an experimental setup which can visualize droplet sheet formation and fragmentation. The mechanical impact of droplets on a solid surface shows the same expansion dynamics as for laser-droplet impact, therefore the development of an experimental setup for droplet impact on a solid surface will be explored [7]. In chapter 2, the theoretical framework for dynamic similarity allowing for this comparison of different fluid flows will be presented. For droplet-pillar impact, quantities that govern the Weber number include droplet diameter and velocity. Therefore, the theory for droplet velocity, of water droplets free falling through air, will also be addressed in chapter 2. Next, the imaging techniques and the image analysis method will be described in chapter 3. Finally, the development of two experimental setups will be described, chapter 4 is dedicated to the development of a setup for millimeter scale studies. The realization of the millimeter setup provided useful insights for the development of the micrometer scale setup, which is described in chapter 5.

Chapter 2

Theory

2.1 Dynamics of fluid flows

A liquid droplet, falling through air, can theoretically be described as a fluid flowing past a stationary sphere. Figure 2.1a shows an ideal flow, with velocity v past a rigid sphere of diameter d. For an ideal flow, streamlines remain unchanged before and after the sphere. In general, the dynamics of fluid flows is governed by the Navier-Stokes equation of motion:

$$\rho \frac{\partial \boldsymbol{v}}{\partial t} + \rho(\boldsymbol{v} \cdot \nabla)\boldsymbol{v} = -\nabla \boldsymbol{p} + \rho \boldsymbol{f} + \eta \nabla^2 \boldsymbol{v}, \tag{2.1}$$

with ρ the density of the fluid, $\boldsymbol{v}$ the velocity field of the fluid, $\boldsymbol{p}$ the pressure field of the fluid, $\boldsymbol{f}$ the externally applied force on the fluid, and η the dynamic viscosity of the fluid. The Reynolds number quantifies the ratio between the viscous term ($\eta \nabla^2 \boldsymbol{v}$), and the inertia term ($\rho(\boldsymbol{v} \cdot \nabla)\boldsymbol{v}$) in Equation 2.1. In case of a fluid flow past a rigid sphere, the Reynolds number Re is defined as

$$Re = \frac{\rho v d}{\eta} \tag{2.2}$$

Experiments have shown that, for water droplets falling through air, the flow around a micrometer sized droplet is described by low Reynolds numbers ($Re < 4$), and that millimeter sized droplets fall into the moderate Reynolds number regime ($80 < Re < 3 \cdot 10^5$) [8]. At low Reynolds numbers viscous forces dominate fluid motion. But at high Reynolds numbers inertia forces are dominant. In the extreme case of $Re \ll 1$ the inertia terms in Equation 2.1 can be ignored, and the equation reduces to

$$\nabla \boldsymbol{p} = \eta \nabla^2 \boldsymbol{v}, \tag{2.3}$$

which is known as Stokes' solution. Although this solution is theoretically only valid for $Re \ll 1$, experiments show that it remains fairly accurate for $Re \leq 1$ [8].

When $Re > 1$ the upstream (flow in front of the sphere) and downstream (flow behind the sphere) streamlines start to become asymmetric, which is illustrated in Figure 2.1b. At these Reynolds numbers, the sphere cannot be considered as a stationary object, and inertia effects need to be included to account for advective acceleration. In Stokes's solution, these effects are not taken into account because the inertia term ($\rho(\boldsymbol{v} \cdot \nabla)\boldsymbol{v}$) is ignored completely. In Oseen's approximation, this term is approximated by a linear function, to account for the effect of advective acceleration at small Reynolds numbers [9]. As inertia forces become more dominant, the streamlines become more asymmetric, and Oseen's approximation breaks down as well. This asymmetry originates from the 'no-slip' boundary condition at a fluid boundary: for a fluid-solid interface, the fluid at the boundary assumes the velocity of the solid. As a result, a vorticity (rotation of the fluid) is created at the surface of the sphere. In Stokes' solution vorticity is assumed to be diffused in the fluid, resulting in uniform streamlines.

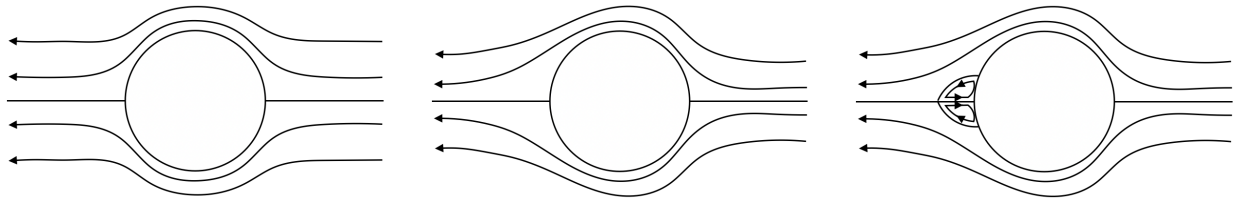

(a) (b) (c)

Figure 2.1: Fluid flow past a rigid sphere for low Reynolds numbers for three different ranges of Re. In the case of $Re < 1$ (a) the streamlines around the sphere are symmetric. Vorticity at the fluid boundary is diffused such that no vortices are created, and the dynamics of the fluid flow can be described by the Stokes' solution. At $1 < Re < 4$ (b) the flow is still axis-symmetric, but inertia effects cause the streamlines before and after the sphere to become asymmetric. Oseen's solution accounts for these small inertia effects. For the case of $Re > 4$ (c) the streamlines behind the sphere are separated by an enclosed vortex ring. This separation region is the result of vorticity being advected in the fluid creating two vortices behind the sphere.

However, at $Re > 4$, vorticity is advected, forming a separation region behind the sphere. This region consists of two vortices, which are contained by a separate streamline, as seen in Figure 2.1c. The streamlines become more asymmetric and Oseen's linear approximation of the advective acceleration also breaks down.

As the Reynolds number increases, the separation region increases in width and length. At $Re > 40$ the wake of the sphere, located behind the separation region, begins to destabilize. At this point vortices of opposite rotation are created periodically in the wake, creating a vortex street which moves with the sphere. When $Re > 80$, the vortex street starts to interact with the vortices in the separation region, causing the flow to become unsteady, which is illustrated in Figure 2.2. For $Re < 200$, the sphere's wake remains laminar, but at higher Reynolds numbers, it transitions to turbulent. This turbulent wake cause the fluid boundary layer around the sphere to detach from its surface. Until the critical Reynolds number $Re_{crit} = 3 \cdot 10^5$, the flow around this boundary layer can still be considered laminar. In Section 2.2, a theoretical framework is defined to analyze droplet velocity at different length scales, which shows the influence of various flow regimes.

The occurance of the Reynolds number in the Navier-Stokes equation is an example of dynamic similarity of fluid flows, which is fundamental to fluid dynamics. The Navier-Stokes equation can be written in non-dimensional form, such that several dimensionless parameter groups arise. These groups are the so-called similarity parameters. Because the Navier-Stokes equation has a unique solution, fluid flows with identical similarity parameters will exhibit the same motion. For example, fluid flows with identical Reynolds numbers, but different length scales, show the same dynamic behavior. The concept of dynamic similarity is extensively used in experimental fluid dynamic studies [10]. Not only experiments at different length scales can be compared, dynamic similarity can be used to compare fluid flows with different velocities, pressures, and densities.

Like the Reynolds number, all similarity parameters have their own physical interpretation. The Reynolds number is used to predict the transition of a fluid flow, from laminar to turbulent. There are two more similarity parameters which are relevant here. First of all, the ratio between surface tension and inertia forces, which is quantified by the Weber number We, is defined as

$$We = \frac{\rho v^2 d}{\sigma}. \tag{2.4}$$

At high Weber numbers, droplets are easily deformed by acceleration or deceleration, since inertial

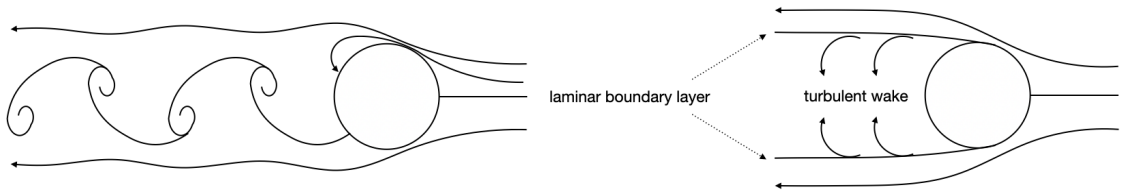

(a) (b)

Figure 2.2: Fluid flow past a sphere for moderate Reynolds numbers $80 < Re < 3 \cdot 10^5$. In the case of $80 < Re < 200$ a vortex street is created in the wake of the sphere, which is still considered laminar. At $Re > 200$ the wake becomes turbulent causing the fluid boundary layer to detach from the sphere. Until the critical Reynolds number $Re_{crit} = 3 \cdot 10^5$ the flow around the separated boundary layer is still laminar.

forces dominate. The Weber number can predict the amount of expansion of a droplet after impact on a pillar. It has been shown that the droplet's radial expansion scales with the Weber number as

$$\frac{r - r_0}{r_0} = 0.12\sqrt{We}, \tag{2.5}$$

with r_0 the original droplet radius and r the expanded droplet radius [11]. The ratio between viscous forces, inertia forces and surface tension forces is quantified by the ratio between Weber and Reynolds number. This similarity parameter is referred to as the Ohnesorge number Oh, which is defined as

$$Oh = \frac{\sqrt{We}}{Re} = \frac{\eta}{\sqrt{\rho\sigma d}}. \tag{2.6}$$

2.2 Droplet velocity

To study how droplets deform upon impacting a solid surface, the Weber number is the most relevant similarity parameter. The comparison of droplet deformation at micrometer and millimeter scales, requires a similar Weber number for both experiments. Equation 2.4 shows that the Weber number is strongly influenced by droplet velocity. Therefore, it is important to define a theoretical framework which can be used to predict droplet velocity at different length scales. As a droplet falls through air, it experiences two counteracting forces: gravitational force F_g and drag force F_d. When these forces are balanced, there will be no net acceleration, and the droplet reaches a constant velocity. The gravitational force on a sphere with density ρ_s falling through a fluid of density ρ_f, can be determined by considering the difference in weight between the sphere and the displaced fluid:

$$F_g = \frac{\pi d^3 g(\rho_s - \rho_f)}{6}. \tag{2.7}$$

The drag force consists of two components: skin friction and pressure drag. Skin friction originates from the viscosity of the fluid, whereas pressure drag originates from the difference in fluid pressure around an object [9]. The drag force is defined as

$$F_d = \frac{1}{8}\rho v^2 d^2 \pi C_d, \tag{2.8}$$

where C_d is the drag coefficient, which depends on the object geometry and the type of flow. For solid spherical objects, the drag coefficient can be expressed as a function of the Reynolds number:

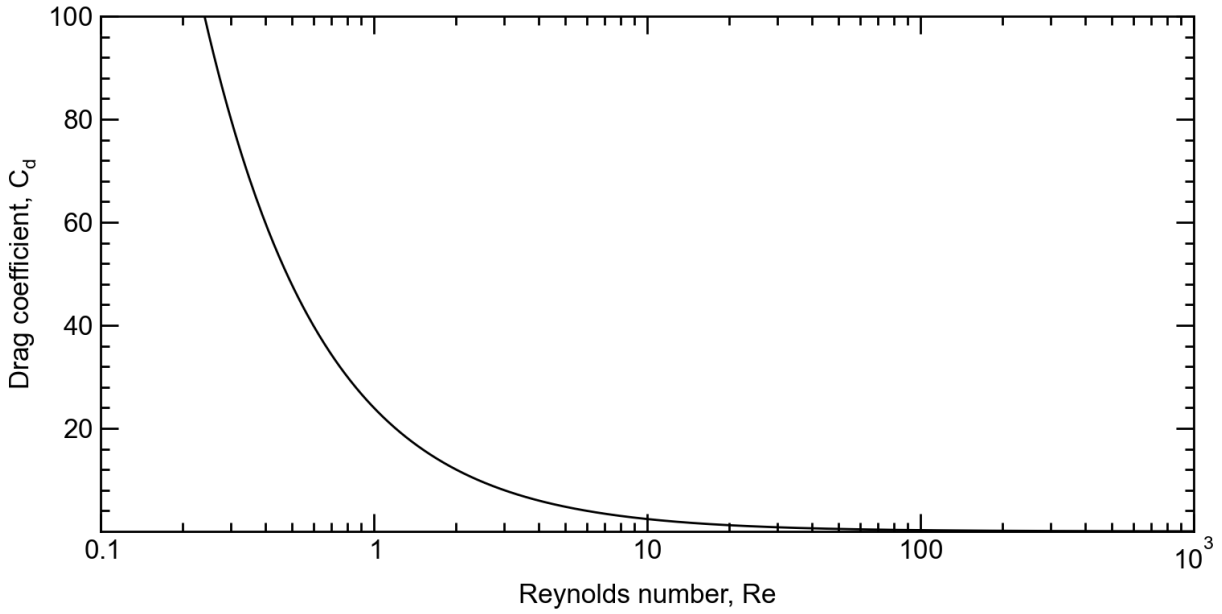

Figure 2.3: Dependence of the drag coefficient on the Reynolds number, for Stokes' solution ($C_d = \frac{24}{Re}$) of fluid flow past spherical objects, in the range of Re = 0.1 − 1000.

$C_d = C_d(Re)$. An illustration of the dependence of the drag coefficient on the Reynolds number, in the range of 0.1-1000, is given in Figure 2.3, where C_d is given by Stokes' solution ($C_d = \frac{24}{Re}$). In the low Reynolds number regime, it is determined analytically using Stokes' solution ($Re < 1$) or Oseen's approximation ($1 < Re < 4$). At moderate Reynolds numbers, no analytical solution exists, requiring an empirically determined function [12].

Terminal velocity of micrometer sized droplets

Drag force can be expressed in terms of the Reynolds number, by using Equation 2.2 and Equation 2.8:

$$F_d = \frac{C_d Re}{24} 3\eta\pi d v. \tag{2.9}$$

For Stokes' solution, where $C_d(Re) = \frac{24}{Re}$, Equation 2.9 reduces to

$$F_d = 3\pi\eta d v, \tag{2.10}$$

which is also known as Stokes' law of resistance [9]. Equating Equation 2.10 and Equation 2.7 gives

$$3\pi\eta d v_t = \frac{\pi d^3 g(\rho_s - \rho_f)}{6}, \tag{2.11}$$

where v_t is the terminal velocity. Rewriting this equation in terms of v_t gives

$$v_t = \frac{g d^2(\rho_s - \rho_f)}{18\eta}. \tag{2.12}$$

To account for small inertia effects due to the fluid's advective acceleration, Oseen's approximation

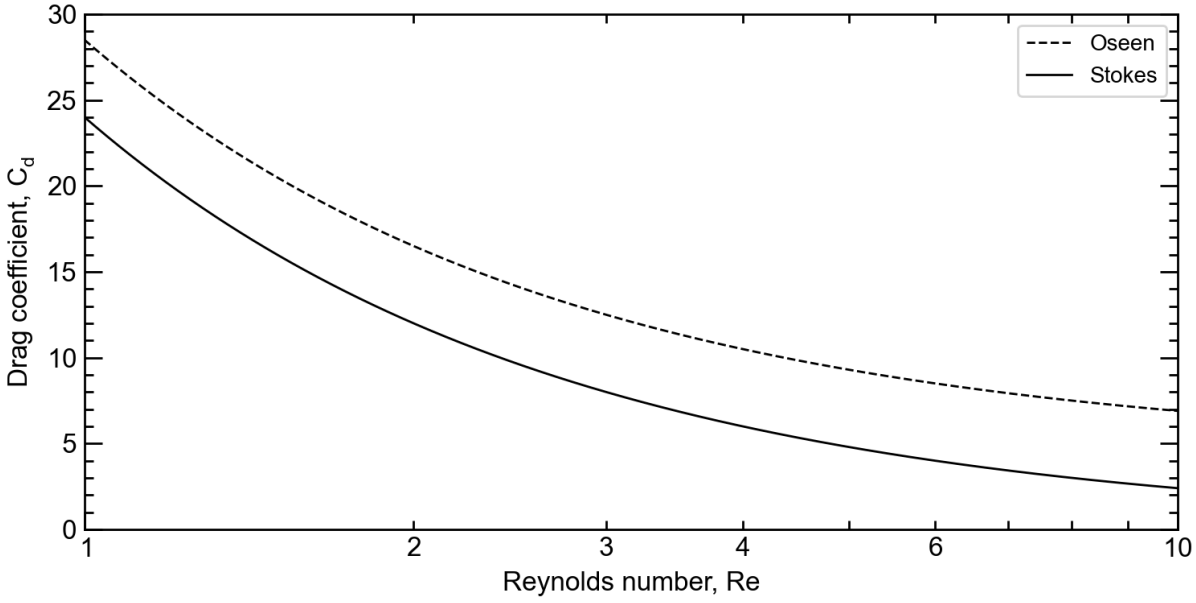

Figure 2.4: The difference in drag coefficient for Stokes' solution (solid line) and Oseen's approximation (dashed line) as a function of the Reynolds number. Due to the inclusion of (linear) advective acceleration terms, the drag coefficient for Oseen's approximation is larger than for Stokes's solution.

can be used to correct Equation 2.12. For Oseen's approximation the drag coefficient is given by

$$C_d = \frac{24}{Re}\left(1 + \frac{3}{16}Re\right). \tag{2.13}$$

Correcting Equation 2.12 using Equation 2.13 gives

$$v_t = \frac{gd^2(\rho_s - \rho_f)}{18\eta}\left(1 + \frac{3}{16}Re\right). \tag{2.14}$$

The difference between the drag coefficient for Stokes' solution and Oseen's approximation are shown in Figure 2.4. To account for the difference between a liquid droplet and a rigid sphere, Equation 2.14 should also be corrected. At low Reynolds numbers, the drag coefficient for water droplets is smaller than for rigid spheres [13]. The fluid flow within a liquid drop accounts for this difference. Liquid droplets can be described as slowly moving bubbles in a viscous flow. For such a bubble, the analytical solution to the Navier-Stokes equation was determined by Hadamard–Rybczynski [14]. The drag coefficient, for a liquid droplet falling in air, is given by

$$C_d = \frac{8}{Re}\frac{3\kappa + 2}{1 + \kappa}, \tag{2.15}$$

with $\kappa = \frac{\eta_d}{\eta_a}$ the ratio between the droplet's viscosity η_d and the viscosity of air η_a. Using Equation 2.15 to correct Equation 2.12 gives the final equation for terminal velocity of micrometer sized droplets falling through air:

$$v_{t_{\mu m}} = \frac{gd^2(\rho_d - \rho_a)}{6\eta_a}\left(1 + \frac{3}{16}Re\right)\frac{1 + \kappa}{3\kappa + 2}. \tag{2.16}$$

Terminal velocity of millimeter sized droplets

For $80 < Re < 3 \cdot 10^5$, Edwards et al. [15] empirically determined the function $C_d(Re)$:

$$C_d = 12Re^{-0.5}. \tag{2.17}$$

Liquid droplets are susceptible to shape distortion, affecting the pressure drag component of the drag force. At moderate Reynolds numbers drag force consists mainly of pressure drag, such that the drag coefficient of water droplets is actually higher than for rigid spheres [13]. Due to aerodynamic pressure differences at the droplet surface, larger droplets are stretched in the horizontal direction, which results in a larger surface area of the droplet. For smaller droplets, the surface tension force is strong enough for the droplets to remain spherical. The correction factor due to shape distortion C_{sd}, which is empirically determined by van Boxel [16], is given by

$$C_{sd} = 1 + \mathrm{a}(We + \mathrm{b})^{\mathrm{c}} - \mathrm{ab}^{\mathrm{c}}, \tag{2.18}$$

with a = 0.013, b = 2.28 and c = 2.12. Using Equations 2.7 and 2.8, and correcting for the effect of shape distortion, we obtain the final equation for terminal velocity $v_{t_{mm}}$ of millimeter sized droplets falling through air:

$$v_{t_{mm}} = \frac{gd^2(\rho_d - \rho_a)}{18\eta_a} \frac{24}{C_d C_{sd} Re} \tag{2.19}$$

Chapter 3

Experimental methods

3.1 Stroboscopic & shadowgraphy imaging techniques

Visualizing droplet dynamics with high spatial and temporal resolution requires the use of stroboscopic imaging [17]. This imaging technique uses flash photography to capture parts of a fluid dynamic process. Due to the reproducibility of the process, a consecutive image sequence of these parts can be used to capture the full process. These images are recorded by delaying the consecutive recordings by a certain fixed time interval (delay time), allowing for short times between frames. Capturing droplet dynamics at the micrometer scale requires a camera with a frame rate of the order of 10^8 fps, which exceeds the limits of available high-speed systems [17].

To determine the requirements of the imaging system, we must consider how the spatial and temporal resolution of the experiments relate to the criteria for achieving optimal visualization. Three key parameters must be considered: interframe time, exposure time, and magnification of the imaging system. The interframe time refers to the time between two successive frames and is related to the timescale of the event. In stroboscopic imaging, it is determined by the delay time, which must be short enough to capture the full dynamic process. For droplet dynamics at the micrometer scale, a minimum delay time in the order of nanoseconds ($\sim$ 10 ns) is required. The exposure time, which is defined as the time each image frame is exposed to an object, is set by the camera's shutter speed or the duration of a light pulse. The magnification of an imaging system is related to the ratio between the pixel size of the camera's imaging sensor and the pixel size in the resulting image frame. To avoid undersampling, the magnification should be chosen so that the Nyquist criterion is fulfilled: at least two pixels must lie between the product of the spatial resolution R_s and the magnification (M) [17]. This determines the minimum magnification as

$$M > 2r_p/R_s, \tag{3.1}$$

here r_p is defined as the pixel size of the imaging sensor. To capture a high quality image of a moving object, the imaging system should be designed to minimize motion blur. The displacement in pixels ϵ of an object moving with velocity v within one frame can be defined as

$$\epsilon = \tau M v/r_p, \tag{3.2}$$

where τ is the exposure time. Motion blur is limited when $\epsilon \leq 1$, thus the exposure time must be chosen such that:

$$\tau \leq r_p/Mv. \tag{3.3}$$

Therefore, the exposure time is affected by both the spatial and temporal resolution of the fluid dynamic process. For droplet experiments at millimeter scale, Equation 3.3 estimates that motion blur is limited when $\tau \sim 1 - 100$ µs. In this case the camera's shutter speed can be fast enough, and a continuous light

source can be used to illuminate the droplet. However, for experiments at micrometer length scales, which require $\tau \sim 0.1 - 10$ µs, a pulsed light source is needed to achieve the desired exposure time.

In a shadowgraphy setup, the light source is aligned with a camera. Light reflecting off the droplet's surface causes a decrease in pixel intensity on the camera's imaging sensor. As a result, droplets appear as dark objects against a bright background. Images are analyzed by measuring the difference in pixel intensity (contrast) between the background and the droplet. Ideally, the light source should have a high enough intensity to cover the full dynamic range of the camera sensor, ensuring sufficient contrast. However, light intensity is limited by the exposure time of the imaging system. A certain brightness can be achieved either by increasing the exposure time, allowing more photons to reach the imaging sensor, or by increasing the intensity of the light source. For millimeter-scale experiments, a continuous light source typically provides sufficient intensity to ensure adequate contrast. However, for micrometer-scale experiments, finding a pulsed light source (with enough power at short pulse lengths) to achieve the required intensity can be challenging.

3.2 Image analysis

The study of droplet dynamics requires time-dependent information on the droplet size, position and shape. This section describes the image analysis method used to extract this information. The method is based on the image analysis described by Kurilovich [1], and consists of three main steps. First, the droplet is located within the full image frame, to create a region of interest (ROI) which contains only the droplet. A crop of this ROI is saved as a new image,and converted to a binary image. Finally, the droplet size and position are extracted from the droplet's surface area in this binary image.

Droplets are located within an image frame by using the Hough circle transform function, from the OpenCV package (operated in Python) [18]. This function is designed to detect circles in images, based on the object's edges. First, it finds the edge coordinates of an object, by examining the gradient between two consecutive pixels. If this gradient is a local maximum, it will be seen as an edge point. The coordinates of all these edge points are combined to form the outer edge of an object. Then, the function returns the center coordinates and radius of the circle that best fits the object's outer edge, by using the Hough transform method [19]. However, the values obtained from this function are not

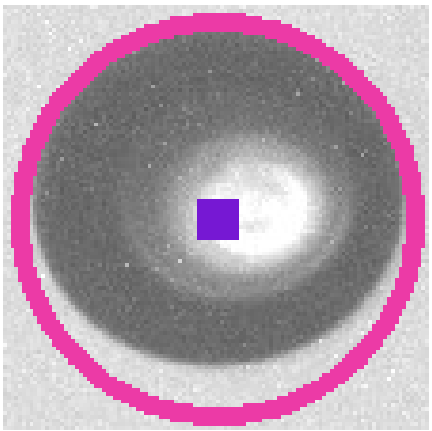

Figure 3.1: Image of a droplet illustrating the inaccuracy of the Hough circle transform function when used to determine droplet size and center position. The function returns a circle with a diameter larger than the droplet (magenta line), and a center position (purple square) which is different from the droplet's center of mass.

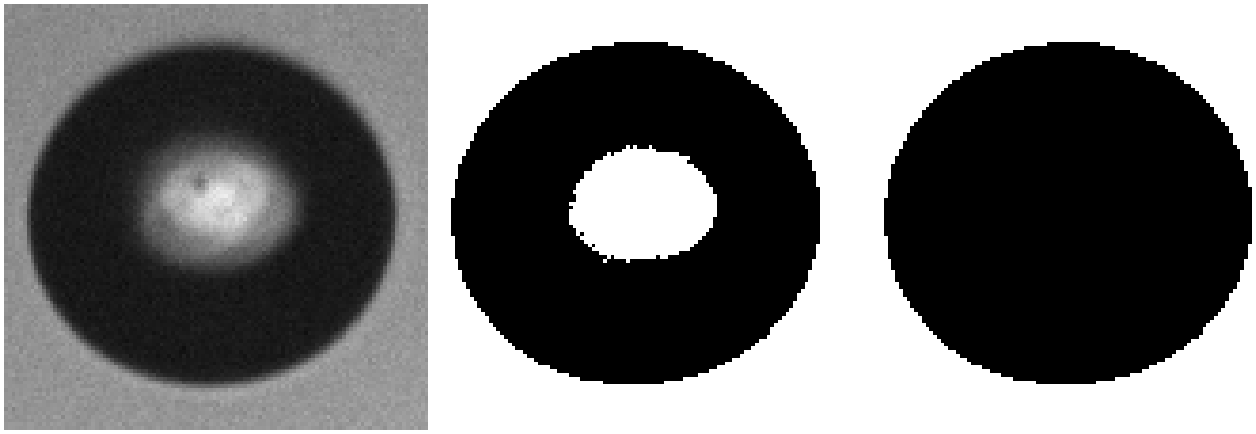

(a) (b) (c)

Figure 3.2: Illustration of the binarization process of cropped droplet images. The original cropped image (a), is turned into a binary image (b). Correcting for the area of increased light intensity in transparent liquid droplets gives the final binary image (c).

accurate enough for data analysis. Inaccuracies arise from the function over- or underestimating the radius of non-spherical droplets, which is illustrated in Figure 3.1. Moreover, the Hough transform function returns the droplet radius by means of a one dimensional analysis. Consequently, the uncertainty in droplet diameter is directly proportional to the pixel size: $\sigma_d \sim r_p$. When the droplet diameter is determined using a 2D analysis based on the droplet area, the uncertainty is proportional to the square root of the pixel size, $\sigma_d \sim \sqrt{r_p}$, resulting in a significantly smaller uncertainty in droplet diameter. Therefore, the initial values for droplet diameter and center positions, obtained from Hough circle transform function, are only used to create a ROI containing the examined droplet. An example of the resulting cropped image is shown in Figure 3.2a.

Next, the cropped images will be converted into binary images. To create a binary image, all pixel intensity values in a grayscale image are evaluated. Each value below a chosen threshold intensity will be set to 0, and each value above the threshold is set to 1. The threshold value varies between imaging systems and depends primarily on light intensity. Therefore, it will be addressed in more detail when describing the different imaging systems for micro- and millimeter experiments.

One challenge to deal with, when working with droplets of transparent liquids, is an area of increased light intensity in the droplet center. In transparent liquids, like water, light is transmitted through the air-water interface, where light at low incident angles is transmitted more than at high incident angles. Due to the spherical shape of droplets, the incident angle of a parallel light beam varies over the droplet surface: the incident angle (with respect to the surface normal) increases when moving away from the droplet center. Therefore, more light will be transmitted through the droplet's center, resulting in an area of increased light intensity. Moreover, due to refraction all transmitted light will be focused towards the center. After binarization, the area of increased light intensity creates a 'hole' in the droplet's center. Filling in these 'holes' in the binary images is the final part of the binarization process, the final image can be seen in Figure 3.2c.

The last step of the image analysis consists of extracting droplet properties from the binary images. First, the droplet area is computed by determining the amount of black pixels in the binary image. Then the droplet diameter d is extracted, by assuming the droplet area can be approximated by the area of a perfect circle: $d = 2\sqrt{area/\pi}$. The droplet position is defined as the position of its center of mass, which can be extracted directly from the binary images in terms of x,y coordinates.

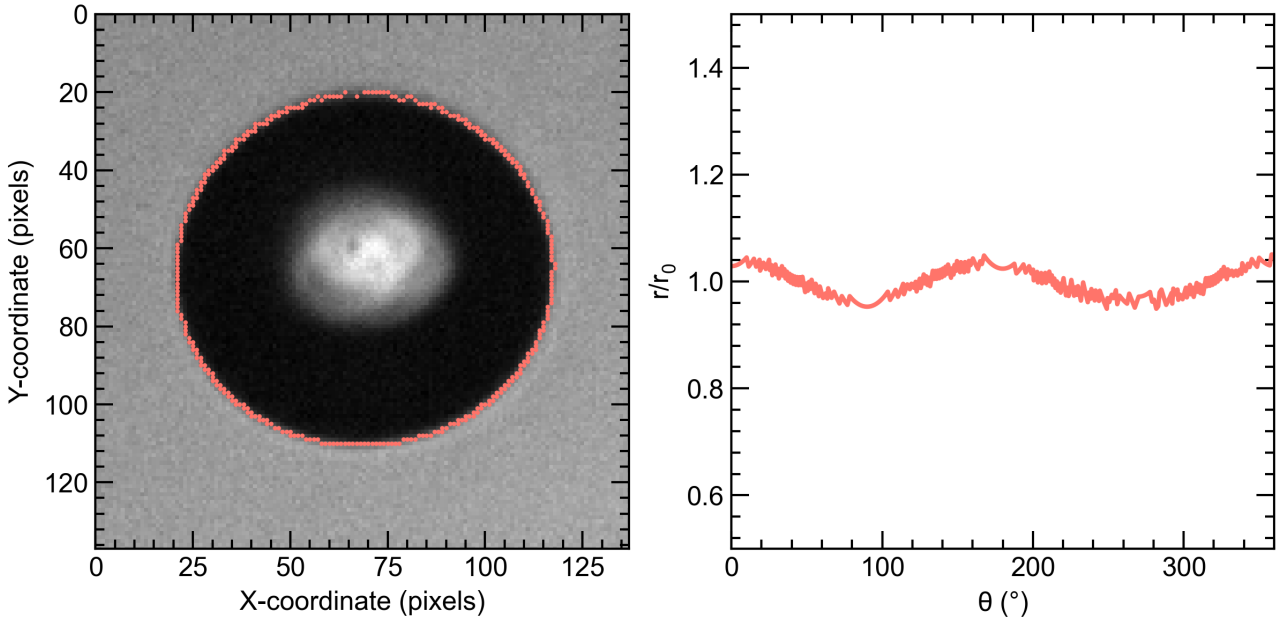

Figure 3.3: Analysis of the droplet shape, which is represented by the droplet outline. On the left side, edge coordinates of droplet outline are plotted on top of the droplet image. Polar representation of these edge coordinates are shown in the plot the right side, where r is normalized by the assumed droplet droplet radius r_0. Note that for a perfect circle, with constant radial distance r, the plot on the right side would simply be a horizontal line.

An analysis of the droplet shape can give some insight into the accuracy of the 'perfect circle' approximation of the droplet area. The droplet's shape is described by the outline of the droplet's surface, which can be found by using an edge detection algorithm. For the droplet shown in the left panel of Figure 3.3, the edge coordinates of the droplet are expressed in terms of polar coordinates (r, θ). Here r is the radial distance from the droplet center, and θ the angle with respect to the droplet's horizontal center axis, where θ is defined in the anticlockwise direction with $\theta = 0$ at the right side of the droplet's horizontal axis. The radial distance is normalized to the assumed droplet radius $r_0 = \frac{1}{2}d$ of a perfect circular droplet. Figure 3.3 shows that the droplet is slightly stretched along the vertical axis, deviating slightly from the 'perfect circular' shape. The area of this droplet can be computed by integrating the radial distance along the droplet surface. Comparing this value to the area of a perfect circle, it can be shown that there is 0.5 % deviation. Inaccuracies that arise due to uncertainty in camera calibration and due to the spatial resolution of the camera will exceed this uncertainty due to shape distortion. Therefore, even for slightly deformed droplets the 'perfect circle' approximation is accurate enough.

Chapter 4

Experimental setup at millimeter scale

First we commissioned a setup to visualize droplet dynamics at millimeter scale. The spatial and temporal resolution which is required for the imaging of millimeter-sized droplets is lower, due to the larger length scale (compared to the micrometer length scale). That setup will involve the same imaging techniques, such that the development of a millimeter setup can be used to gain experience with imaging systems, trigger systems, and imaging analysis methods. In the first part of this chapter, the theory of millimeter droplet formation from a capillary tube will be described. This is required to estimate the range of droplet sizes that the setup can effectively examine. Next, a numerical model is introduced which theoretically predicts the droplet velocity. Then, the details of the experimental setup and image analysis method are described. The obtained data will be evaluated against their predicted values.

4.1 Droplet formation

By pushing liquid through a capillary tube at a constant flow rate, millimeter size droplets can be generated. When substituting the capillary outer diameter d_o for the droplet diameter, and the flow rate q_v for the droplet velocity in Equation 2.4, the tube's flow can be characterized by the Weber number. At low Weber numbers, droplets with constant size will periodically detach from the end of the capillary: liquid accumulates at the capillary tip until it detaches from the tube forming a spherical droplet [20]. Droplets are formed when the gravitational force on the accumulated liquid is strong enough to overcome the surface tension force, which originates from adhesion between water and the capillary tube. The force balance between gravity and surface tension gives the following dependence of the droplet diameter d on the capillary outer diameter d_o:

$$d = \left(\frac{6 d_o \sigma}{\rho g}\right)^{\frac{1}{3}}, \tag{4.1}$$

with ρ the liquid density, σ the surface tension, and g the gravitational constant. In Equation 4.1 a few factors affecting the droplet diameter are not considered. When a droplet detaches from a capillary tube, a fraction of the accumulated liquid remains attached to the tube surface. The volume of the detached droplet is smaller than the total volume of the accumulated liquid, leading to a smaller droplet diameter. To account for this effect, the Harkins-Brown correction factor f is introduced in Equation 4.1, which corrects for the deviation in actual droplet volume compared to the ideal case [21, 22]. To account for additional effects of gravity, surface tension, momentum flux, and added volume during necking and detachment, two additional terms are introduced, such that the theoretical prediction for the droplet diameter is given by [20, 22, 23]:

$$d = \left(f\left[\frac{6 d_o \sigma}{\rho g} + 42.84\left(\frac{\sigma d_o^2 q_v^2}{4\rho g^2 \pi^3}\right)^{\frac{1}{3}} - \frac{32 q_v^2}{\pi^2 g d_o^2}\right]\right)^{\frac{1}{3}} \tag{4.2}$$

4.2 Numerical model for milli-droplet velocity

For characterization of the setup, experimental obtained values for droplet velocity will be evaluated against theoretical predictions. The evaluation of Equation 2.19 is not straightforward, due to the appearance of the Reynolds number and Weber number. Also, millimeter sized droplets (in the range of d ≈ 2.5 – 3.5 mm) need more than 10 m to obtain their terminal velocity, as can be seen in Figure 4.1. The setup was not developed to allow for a falling distance of 10 m, which stipulates the need for a model that predicts the droplet velocity before reaching terminal velocity. Velocity as a function of time $v(t)$ can be obtained by considering Newton's second law: $F_{net} = m\frac{\partial v(t)}{\partial t}$. The net force is equal to the difference between gravitational force and drag force: $F_{net} = F_g - F_d$. Since the drag force is a function of velocity, this equation will be a differential equation. Substituting Equations 2.7, 2.9, 2.17 and 2.18 into Newton's second law yields the full differential equation:

$$\frac{\partial v(t)}{\partial t}\frac{\pi d^3 \rho_w}{6} = \frac{\pi d^3 g(\rho_w - \rho_a)}{6} - 3\pi\eta d v(t)\frac{\sqrt{Re(t)}}{2}(1 + \mathrm{a}(We(t) + \mathrm{b})^{\mathrm{c}} - \mathrm{ab}^{\mathrm{c}}), \tag{4.3}$$

where ρ_w is the density of water, ρ_a the density of air, η the viscosity of air, and with a,b,c constants: a = 0.013, b = 2.28 and c = 2.12. Note that Re and We are functions of time, due to the appearance of $v(t)$ in Equations 2.2 and 2.4. Equation 4.3 is solved numerically, the resulting curves for velocity as a function of time, for droplets of d = 2.5 – 3.5 mm, are given in the left plot of Figure 4.1. For all numerical solutions it is assumed that the droplets have no initial velocity. To obtain droplet velocity as a function of the falling distance, the curves for $v(t)$ are integrated by using discrete time steps. The predictions for droplet velocity as a function of falling distance, for droplets of d = 2.5 – 3.5 mm, are shown in the right panel of Figure 4.1.

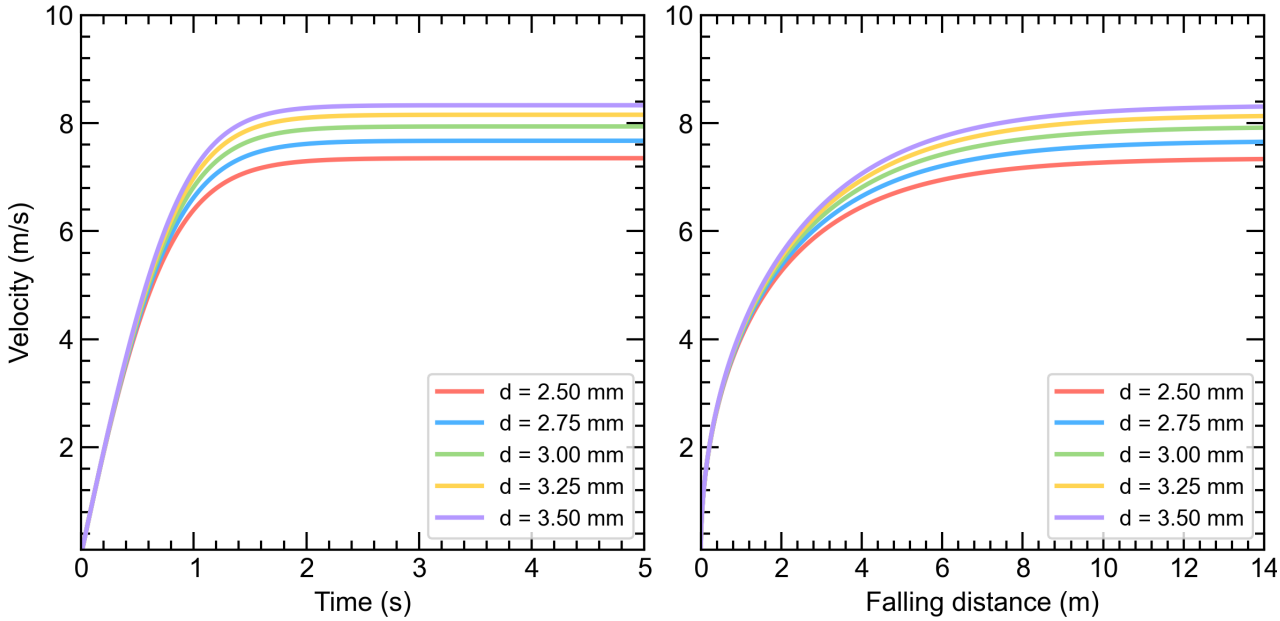

Figure 4.1: Numerical solutions for droplet velocity as a function of time (left) and droplet velocity as a function of falling distance (right), for millimeter sized water droplets in the range of d = 2.5 – 3.5 mm.

4.3 Experimental setup

The setup is designed explicitly to visualize the droplet impact on a similar sized pillar. The impact induces a pressure on the droplet surface, which travels through the droplet and consequently deforms it. The ratio between droplet diameter and pillar size determines the pressure distribution; using a pillar with an equivalent diameter to the droplet diameter will ensure a uniform pressure distribution. Millimeter droplets are generated by a syringe pump (to ensure constant flow), which is connected to a millimeter sized needle. Droplets periodically detach from the needle, which are imaged by the visualization setup. The droplet generator and visualization setup are inspired by the setups designed by Klein [24] and Kurilovich [1], who studied study laser-droplet impact on (millimeter sized) water and (micrometer sized) tin droplets. The droplet diameter can be predicted from Equation 4.2, and mainly depends on the outer diameter of the needle. A mechanical manipulator can be used to adjust the location of the droplet stream, which is necessary for alignment of the visualization setup with respect to the droplet stream.

A schematic overview of the visualization setup is shown in Figure 4.2. The setup includes two main systems: an imaging system and a trigger system. A shadowgraphy imaging system typically consits of a light-sensitive device aligned with the imaging object and a light source. Our imaging setup uses a constant light source combined with a CMOS camera (XIMEA MQ013MG-E2). Images are captured and displayed on a computer using the XIMEA CamTool from the Ximea software package.

The schematic overview in Figure 4.2 illustrates the laser path of a Helium Neon (HeNe) laser, which is aligned with the droplet stream (blue droplet) by using two broadband mirrors. A neutral

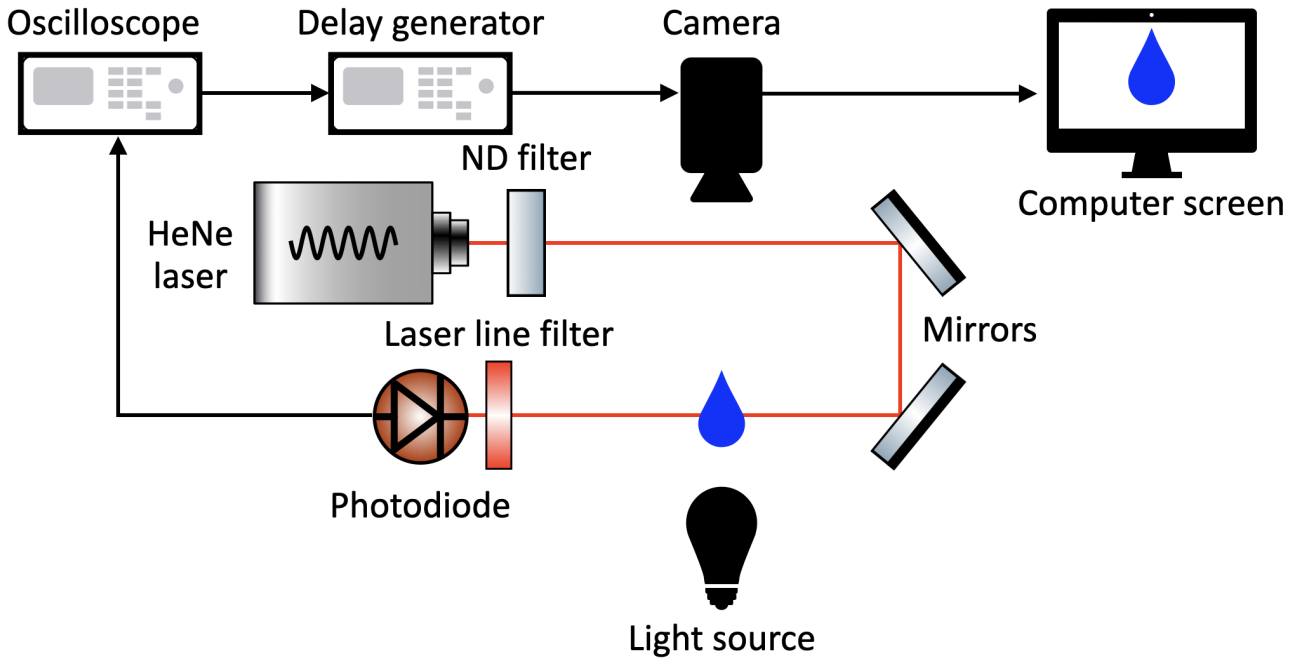

Figure 4.2: Schematic overview of the droplet visualization setup. Droplets that fall through the laser beam path decrease the light intensity that is detected by the photodiode. The decrease in output signal from the photodiode is detected by the oscilloscope, which creates a transfer-to-logic (TTL) pulse. The TTL pulse is passed to the delay generator, which can delay the TTL pulse before transferring it to the camera. Detailed description of different parts of the setup is given in the main text.

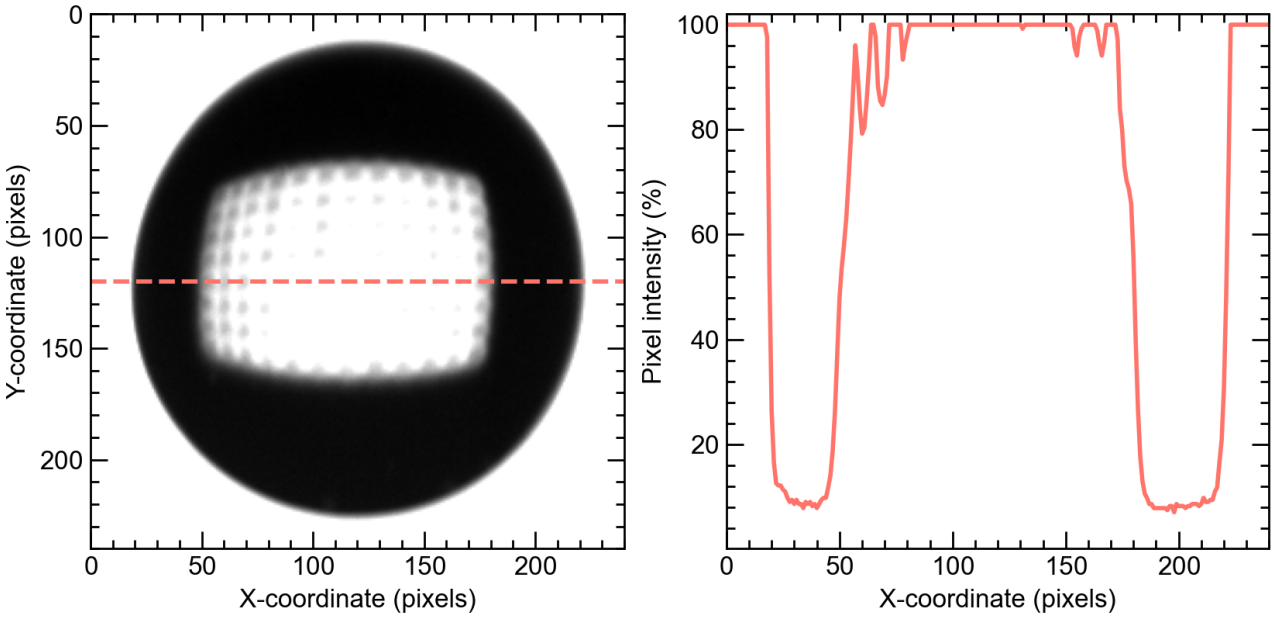

Figure 4.3: Left figure shows a cropped droplet image, illustrating how the droplet appears as a black image on a uniform white background. The plot on the right side of Figure 4.3 shows an evaluation of a row of pixel intensities at the droplet center, corresponding to the horizontal line in the left figure. At the droplet surface the gradient in pixel intensity is highest. In the center region, the pixel intensity increases, due to the effects of refraction and reflection.

density (ND) filter (Thorlabs NE15B) is placed in front of the laser to decrease its output power. At the end of the laser beam path, a photodiode (Thorlabs DET100A2) is placed to detect changes in laser beam intensity. In front of the photodiode, a 633 nm laser line filter (Thorlabs FHL633-5) is placed to eliminate the effect of background light on the photodiode. The output signal of the photodiode is transferred to an oscilloscope (Agilent Technologies DSO6034A 300 MHz) for visualization of the output signal and to create a new trigger signal. When a droplet passes through the laser beam it reflects part of the light, which decreases the photodiode output signal. The oscilloscope is programmed to detect this decrease and create a trigger signal, (TTL pulse) which is passed on to the delay generator (Quantum composers 9520 series). The delay generator can be used to delay any signal it receives, before transferring it to the camera. Every time a droplet passes through the laser beam it triggers the camera, and by adjusting the delay time a stroboscopic image sequence of the droplet's life can be created.

Threshold for image analysis

The image analysis technique, described in Section 3.2, requires the determination of an intensity threshold for binary images. To obtain the threshold, a method described by Yung et al. [25] will be used. This method is based on the assumption that the gradient between two pixels is highest at the droplet outline, such that the pixel intensity value with the highest average (absolute) gradient is most likely to define the droplet outline. That pixel intensity value will then be used as the threshold value for binarization. Our images are grayscale images, with pixel intensity values in the range of 0% (black) and 100% (white). In this method, one would normally subtract a background image from the droplet image to correct for a non-uniform background. But due to the cropping procedure

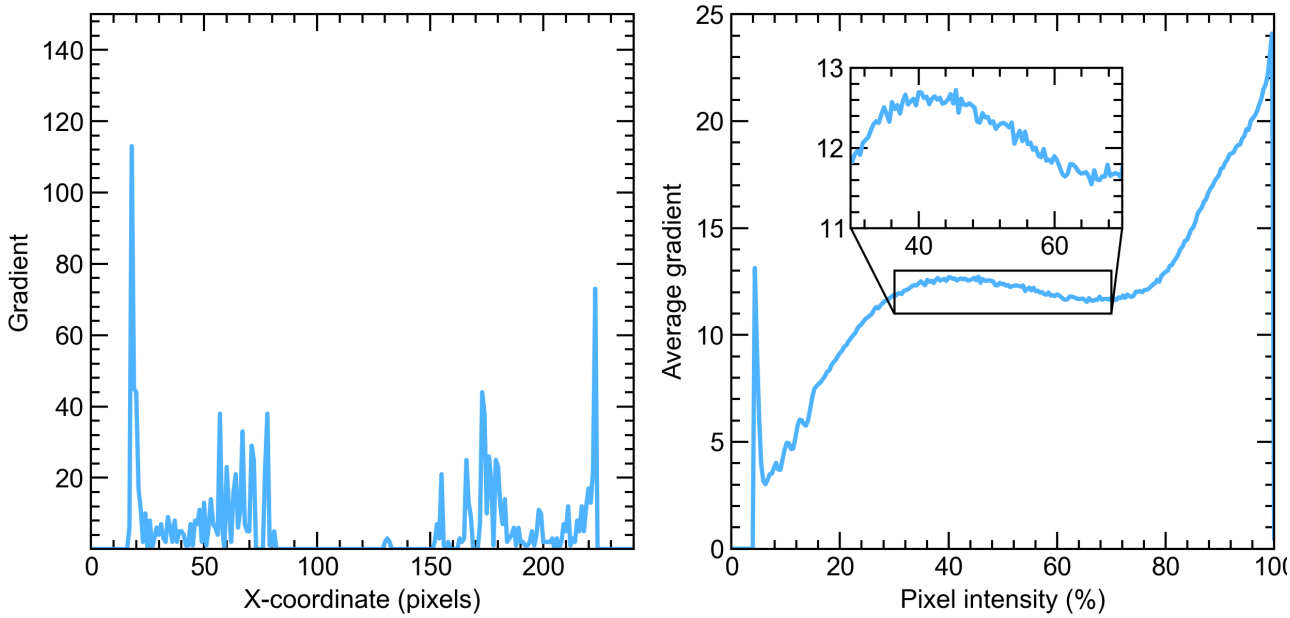

Figure 4.4: The gradient values of a pixel row, indicated by the dashed line in Figure 4.3, are evaluated and shown on the left side. The maximum gradient values are found at the outer edges of the droplet surface. On the right side, a plot of the average gradient values per pixel intensity difference. For threshold determination, only the gradient peak within the 30 – 70% range is considered. The inset shows the gradient peak in this range. The average gradient has a maximum at 45.4%, which will be used as the threshold for binarization.

(Section 3.2) and the uniform white background, no further correction is required.

The plot on the right side of Figure 4.3 shows an evaluation of a row of pixel intensities at y=120 (dashed line in left figure). The outer left and right regions show that the background has a constant value of 100%. At the droplet surface a sharp decrease in pixel intensity appears. In the center region, the pixel intensity increases, due to the previously mentioned effects of refraction and reflection. The plot on the left side of Figure 4.4, where the gradient values correspond to the same row of pixels as in Figure 4.3, shows that indeed the gradient value is highest at the droplet surface. For determination of the average gradient as a function of the pixel intensity, all pixels in a droplet image will be considered, and evaluating multiple images will smoothen the curve such that a clear peak of the average gradient will appear. To obtain the final plot of the average gradient versus the difference in pixel intensity, which is shown on the right side of Figure 4.4, more than 1000 images were analyzed. These images were taken at different time delays and with various needle sizes. The threshold value defines the transition from droplet image (black) to background (white). In the region of 70 – 100%, a peak in average gradient appears because of the transition of background (white) to droplet image (black). Therefore, the gradient peak in this region is not considered when looking for the threshold value. In the range of 0 – 30%, a peak appears at approximately 4%. However, due to the small number of pixels (15) at this intensity, compared to other pixel intensity values ($> 10^4$), this peak is not representative of the correct threshold value. To determine the appropriate threshold, only the gradient peak in the region of 30 – 70% is considered, which is shown in the inset of Figure 4.4. The maximum average gradient value is found at a pixel intensity of 45.4%, which sets the threshold for binarization.

Magnification of the imaging system

The camera has a lens with adjustable focus, magnification and diaphragm. These settings are useful for correct alignment of the camera with the droplet stream. However, both the adjustable magnification and focus influence the total magnification of the imaging system. Also, the distance between the camera and droplet stream adjusts the overall magnification, due to the depth of field of the camera. Therefore, a new camera calibration should be performed when the position of imaging system is adjusted. Calibration can be a lengthy process, since the calibration target has to be placed in exactly the same plane as the droplet stream. To avoid a time consuming calibration procedure, the pillar (which is used for droplet impact) was always kept visible in the image frame. During measurements the pillar is always aligned with the droplet stream, and its size is determined with a 0.01 mm accuracy. The camera's spatial resolution (R_s = 0.03 mm) exceeds the uncertainty in pillar size, making the pillar suitability for calibration.

The distance between the droplet stream and the camera remains constant between measurements due to the fixed position of the laser beam, as only droplets passing through the beam are detected and trigger the camera. Changing the needle in our experimental setup influences the position of the droplet stream. This is corrected by evaluating the photodiode signal: droplets that pass through the center of laser beam cause the sharpest decrease in output signal of the photodiode. Adjusting the needle position accordingly ensures a constant distance between droplet stream and camera. The same principle applies to the pillar, which is used for camera calibration. The pillar's position is adjusted such that the droplet stream hits its center, ensuring the distance between the pillar and camera is kept constant between measurements.

4.4 Setup characterization

Droplet diameter

Droplet diameters are determined for needles with four different outer diameters (d_o= 0.7176 mm, 0.8192 mm, 0.9081 mm, 1.067 mm). To study the effect of tip shape, some needles with the same four outer diameters were carefully flattened. The two different tip shapes are illustrated in Figure 4.5 The droplet diameters of sharp tip shape and flat tip shape needles are plotted against the needle's outer diameter in Figure 4.6, where the outer diameter d_o is approximated by the outer diameter at the needle tube. The theoretical values for droplet diameter, as a function of outer diameter, are given by Equation 4.2.

As expected, the droplet diameter decreases with decreasing outer diameter (see Equation 4.2), and all experimental data seems to follow the same trend as the theory curve. For flat tip shape, the experimental values are all slightly smaller than their predicted values. In a similar study, experimental values were also found to be smaller than predicted by theory [20]. This deviation is attributed to the non-spherical shape of the droplets, incorrect determination of the factor f and experimental errors. In the previously described image analysis method, a non-spherical droplet only causes a 0.5 – 1 % deviation in total surface area of the droplet. Since $d \propto \sqrt{area}$, the error due to a non-spherical shape is neglectable. The threshold value for binarization, which is used in the image analysis to determine droplet surface area, has an influence on the droplet diameter. But an examination of droplet diameter at different threshold values shows this influence is limited to ± 0.01 mm. In another study, Zhang and Basaran [23] identified flaws in the theoretical analysis, explaining the discrepancy between experimental results and Equation 4.2. The relative smaller droplet diameter was attributed to

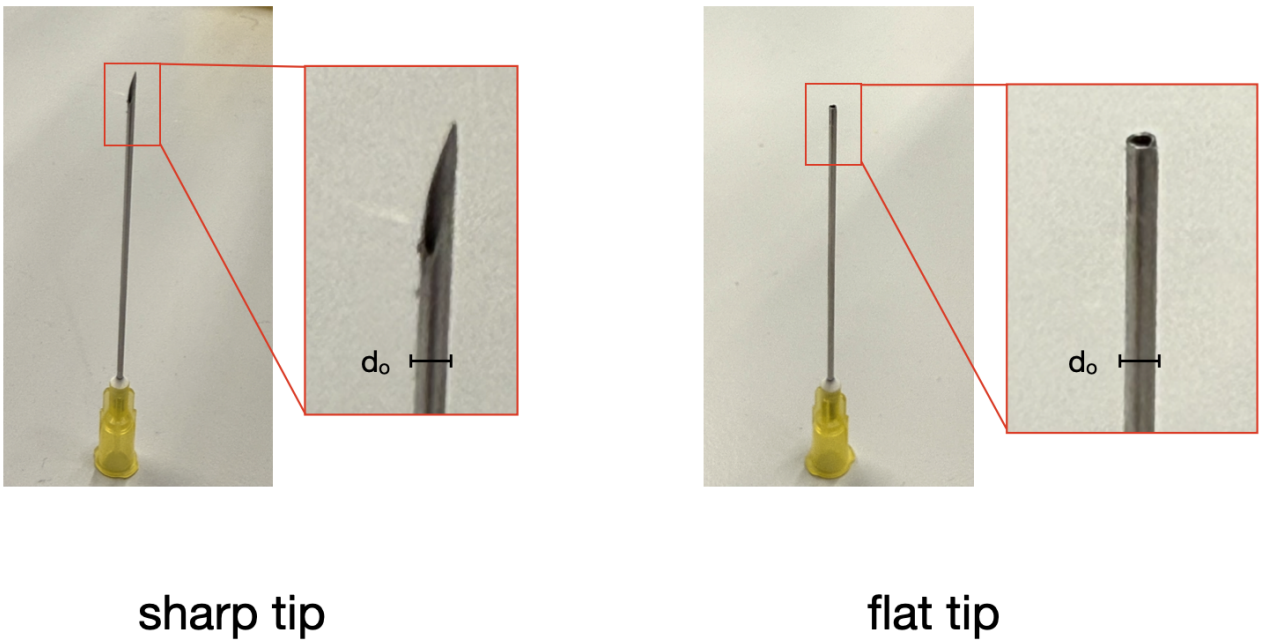

Figure 4.5: Close-up pictures of needles with two different tip shapes: sharp (left) and flat (right). For both tip shapes, the outer diameter d_o is approximated by the outer diameter of the needle tube.

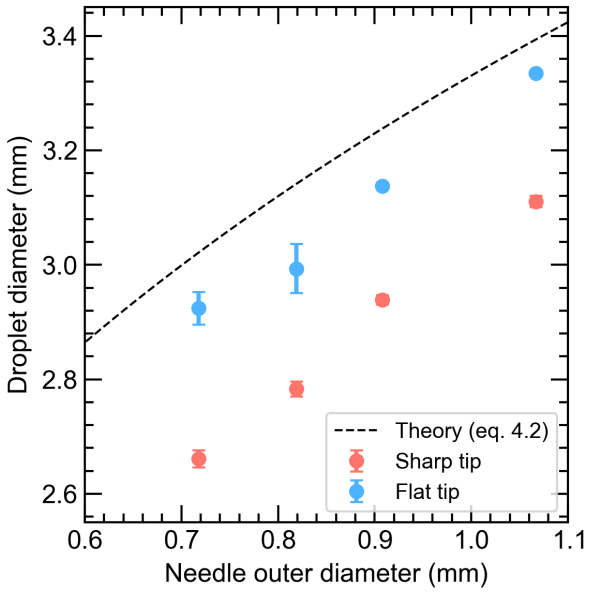

Figure 4.6: Droplet diameter values obtained for needles of different outer diameters (d_o= 0.7176 mm, 0.8192 mm, 0.9081 mm, 1.067 mm) and tip shapes. Flat tip shapes are indicated by blue dots (●) , sharp tip shapes are indicated by red dots (●). Theoretical values (dashed line) are given by Equation 4.2.

the incorrect assumption of static conditions during the drop detachment process, and the assumption of zero wall thickness.

For sharp tip shapes, all droplet diameters are significantly smaller than the predicted ones, and smaller than the values for flat tip shapes. The deviation in droplet size, between sharp tips and flat ones, is attributed to the difference in outer diameter at the needle tip (see Figure 4.5). For the results in Figure 4.6, the outer diameter of the needle tip was approximated by using the outer diameter of the needle. This assumption was made because it was unsure where exactly the droplet would detach from the needle tip. An examination of this detachment process could provide more insight into the actual outer diameter at the droplet detachment location.

Droplet velocity

To obtain the droplet velocity, the droplet position at different delay times has to be recorded. Then the droplet position can be plotted as a function of the delay time, and the velocity is extracted from the slope of a linear fit. Only the velocity in the y-direction (vertical direction) is considered. Droplet velocities at different falling distances (0.12 – 0.62 m) are examined, the obtained values are evaluated against the numerical model described in Section 4.2. The results in Figure 4.6 show that the range of droplet diameters is limited to d = 2.6 – 3.4 mm. Based on the numerical solution for velocities in the range of 0 – 1 m, it is expected that the velocity values in this range lie close together, such that only the velocities for the smallest (d_o = 0.7176) and largest (d_o = 1.067) needles with different tip shapes were examined, the results are shown in Figures 4.7 and 4.8. The experimentally determined droplet diameter (Figure 4.6) for each needle is used as input parameter for the numerical solution. From the results Figures 4.7 and 4.8 it is seen that the numerical model for velocity agrees very well with the experimental values.

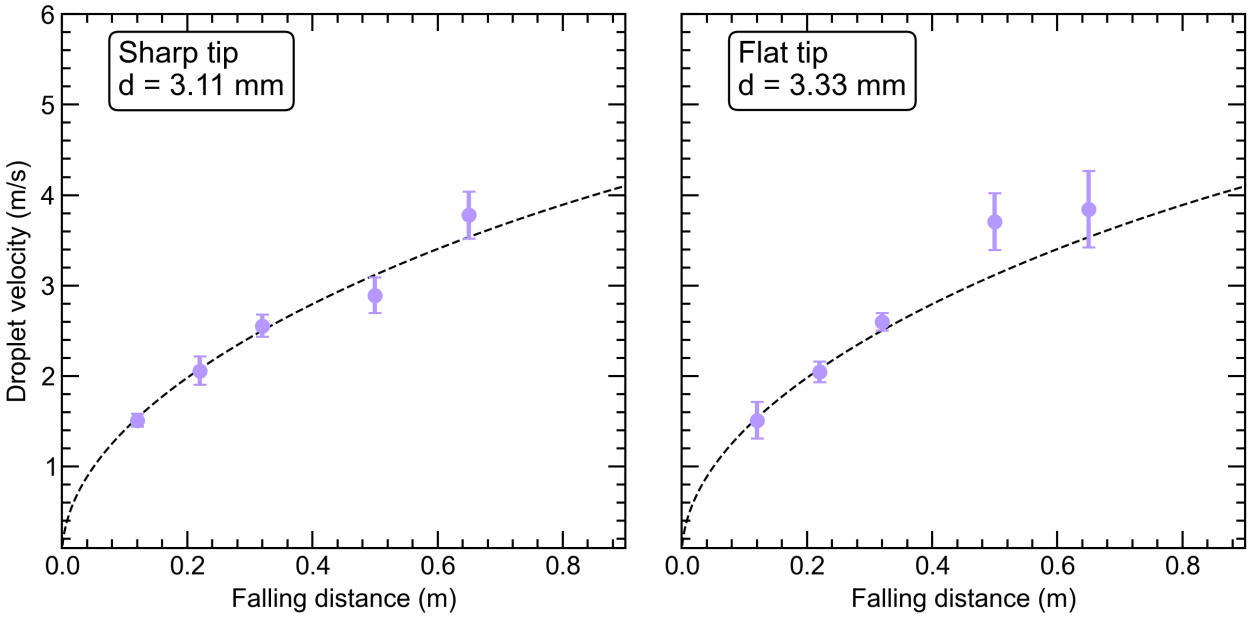

Figure 4.7: Droplet velocity as a function of falling distance for needles with d_o = 1.067 mm and different tip shapes: sharp (left) and flat (right). Experimental values are evaluated against the numerical model for droplet velocity (Section 4.2), with the experimentally determined droplet diameter for sharp tip shape (d = 3.11 mm) and for flat tip shape (d = 3.33 mm) as input parameters (see droplet diameter results in Figure 4.6).

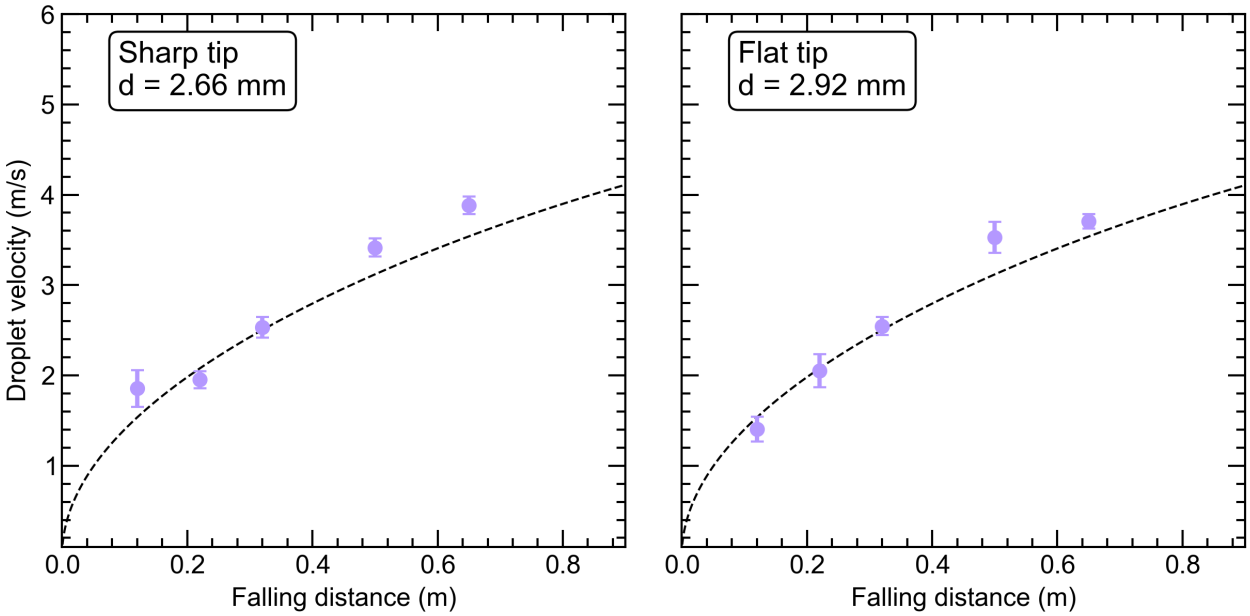

Figure 4.8: Droplet velocity as a function of falling distance for needles with d_o = 0.7176 mm and different tip shapes: sharp (left) and flat (right). Experimental values are evaluated against the numerical model for droplet velocity (Section 4.2), with the experimentally determined droplet diameter for sharp tip shape (d = 2.66 mm) and for flat tip shape (d = 2.92 mm) as input parameters (see Figure 4.6).

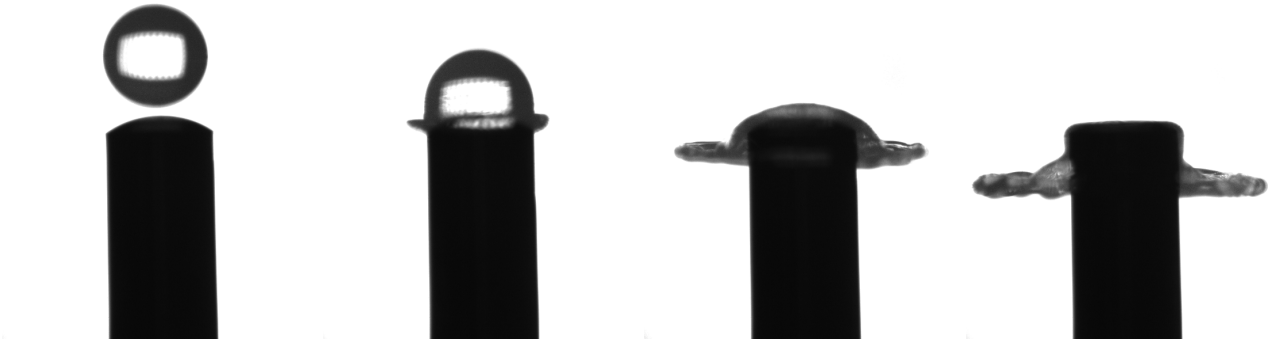

Figure 4.9: Side views of a shadowgraphy image sequence of a millimeter sized droplet impact on a pillar.

Droplet impact on a pillar

Shadowgraph images of droplet deformation upon impact on a pillar have been captured and are shown in Figure 4.9. After impact, the droplet extends radially and a sheet is formed, due to the relative dominance of the inertia force (compared to the surface tension). The amount of radial expansion of the droplet diameter is related to the Weber number, through Equation 2.5. The range of Weber numbers that can possibly be examined with the current setup was determined from the characterization results. Based on these results, the Weber number range, with $\sigma = 7.3 \cdot 10^{-3}$ N/m and $\rho = 997$ kg/m^3, is found to be We = 50 – 550.

4.5 Conclusions

The millimeter setup was characterized in terms of droplet size and droplet velocity. For needles of different tip shapes (sharp and flat) with four different outer diameters (in the range of $d_o = 0.7176$ – 1.067 mm), the droplet diameter was found to be in the range of d = 2.6 – 3.4 mm. The difference in droplet diameter, between needles with flat and sharp tip shapes, is most likely caused by a difference in ”effective” outer diameter at the needle tip. In general, the droplet diameters are slightly smaller than model predictions. For droplet diameters in the range of d = 2.6 – 3.4 mm, at falling distances in the range of 0 – 1 m, the droplet velocity was found to be in the range of 1 – 4 m/s. The droplet velocity can be predicted very well by using a numerical model. From the characterization results for droplet diameter and velocity, the range of Weber numbers was found to be We = 50 – 550. A stroboscopic image sequence, of droplet deformation after impact on a pillar, shows that the setup can effectively visualize droplet deformation at the millimeter scale. The realization of the millimeter setup provides useful insights for the development of a micrometer setup, which will be described in the next chapter.

Chapter 5

Microdroplet setup

5.1 Droplet-on-Demand system

Droplet-on-demand (DOD) systems are commonly used in inktjet applications, to generate micrometer sized liquid droplets. A schematic illustration of the DOD system is shown in Figure 5.1a. The main part of the system consists of a glass capillary, where the liquid inlet is situated at the top of the capillary, which is connected to a liquid reservoir by means of a plastic tube. The bottom end of the capillary is connected to a nozzle, its inner diameter is significantly smaller than the capillary's diameter. A piezo electric actuator surrounds the glass capillary, and deforms upon application of an actuation waveform, which is shown in Figure 5.1b. The actuator can be used to increase or decrease the inner radius of the glass capillary, depending on the polarity of the waveform. The amplitude of the waveform corresponds to the pulse voltage, and the length of the signal corresponds to the pulse width. A positive pulse voltage will decrease the capillary radius, generating a positive pressure wave which travels towards the nozzle. The increase in pressure accelerates liquid towards the nozzle, where

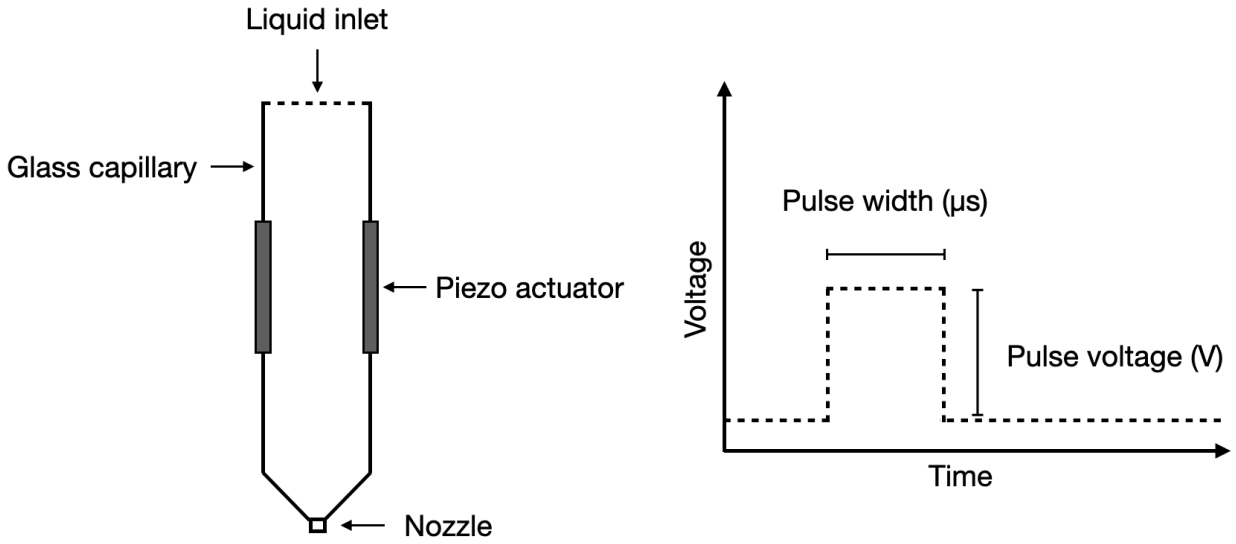

(a) (b)

Figure 5.1: Schematic overview of the main part of a droplet-on-demand system (a). At the liquid inlet, the glass capillary connects to a liquid reservoir by means of a plastic tube, which is bigger than the glass capillary diameter. On the other end, a nozzle with a much smaller diameter is connected to the glass capillary. The piezo actuator is used to increase or decrease the capillary's diameter. The piezo is actuated by a pulsed waveform (b), where the amplitude is set by the pulse voltage, and the duration is set by the pulse width. The illustrated waveform has a positive polarity.

the liquid will be pushed out at the nozzle end. Essentially, liquid is 'squeezed' out of the nozzle. The duration of the piezo deformation, and corresponding duration of the pressure wave, is determined by the pulse width.

Bogy and Talke [26] presented a theoretical analysis of the operation of a DOD system for negative pulse voltage, based on the propagation and reflection of pressure waves inside the glass capillary. First, a negative pulse voltage increases the capillary's diameter, generating a negative pressure on the liquid inside the capillary (Figure 5.2a), which is divided into two waves that travel to both ends of the capillary (Figure 5.2b). At the liquid inlet the low pressure wave is reflected back as a high pressure wave (left side of Figure 5.2c). At the nozzle end, the low pressure wave is also reflected back into the capillary, but without changing from a low to high pressure wave (right side of Figure 5.2c). A high pressure wave is now traveling towards the nozzle end, while a low pressure wave travels towards the liquid inlet. When the negative voltage pulse ends, the piezo actuator contracts causing a second pressure wave (Figure 5.2d). If the application of the second pressure pulse is applied at a time of $t = l/c$, where l is the capillary length and c the acoustic wave speed, the pressure waves induced by the first and second pulse will interact. The high pressure wave traveling to the nozzle will be doubled, while the low pressure wave traveling to the liquid inlet is annihilated (Figure 5.2e). The high pressure wave arrives at the nozzle end at time $t = 3l/2c$, which is when a droplet ejects. Consequently, the timing of the second pressure pulse, corresponding to the pulse width of the actuation waveform, influences both the amplitude and duration of the pressure pulse arriving at the nozzle end. The optimum value for the pulse width is $t_p = l/c$.

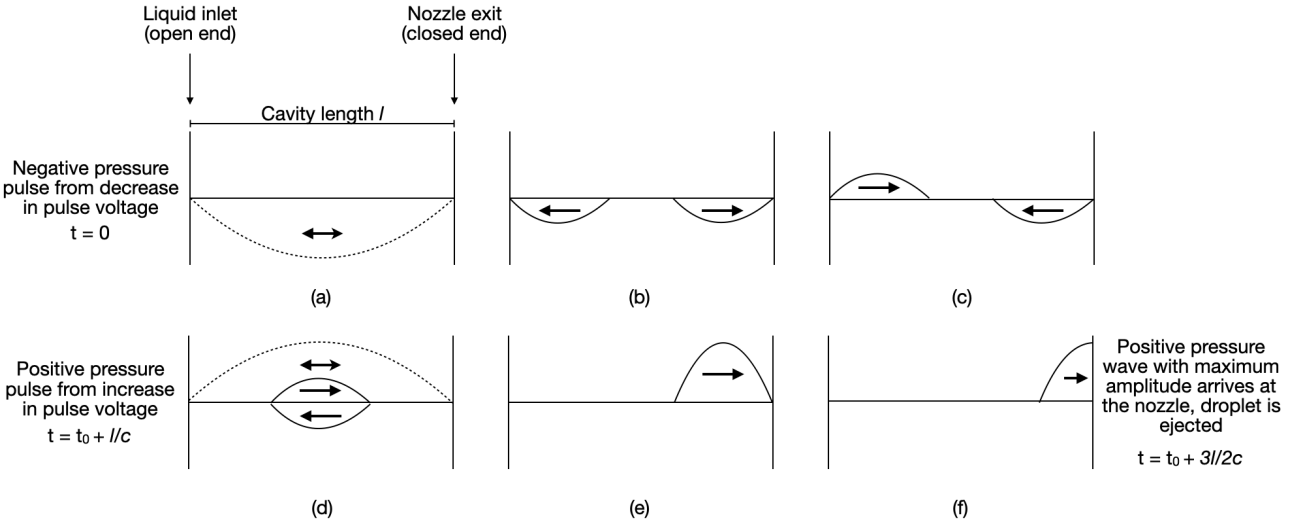

Figure 5.2: Propagation of pressure waves, as a result of the negative pulse voltage. Initial (at t = 0) negative pressure wave is induced by the contraction of the piezo actuator (a), and travels to both ends of the glass capillary (b). The pressure wave reflects at the nozzle end, but changes into a positive pressure wave at the liquid inlet (c). Application of the positive pressure pulse at time $t = t_0 + l/c$ (d), results in the annihilation of the negative pressure wave, and amplification of the positive pressure wave (e). At $t = t_0 + 3l/2c$ a droplet is ejected at the nozzle end (f). The interference of pressure waves for negative pulse voltages results in higher pressure waves (compared to a positive pulse voltage), if the pulse width is optimized such that $t_p = l/c$.

Droplet formation

We will use an image sequence of the microdroplet generation to describe the droplet formation process. First, liquid is pushed out of the nozzle and forms a liquid column, with a radius that is equal to the inner diameter of the nozzle (Figure 5.3a). As long as the fluid velocity at the nozzle exit is high enough, liquid will keep flowing in the column (Figure 5.3b). As the pressure at the nozzle decreases, the fluid velocity at the nozzle exit decreases. The difference in fluid velocity between the column head and the nozzle exit will cause the column to stretch (Figure 5.3c). The fluid velocity at the nozzle exit will continue to decrease, and eventually no liquid will flow into the column anymore. The total volume of the liquid column will remain constant, but the column will continue to stretch due the inertia of the liquid. When a low pressure wave arrives at the nozzle exit, a fraction of the liquid is sucked back into the dispenser head. The fluid flow back into the dispenser head further stretches

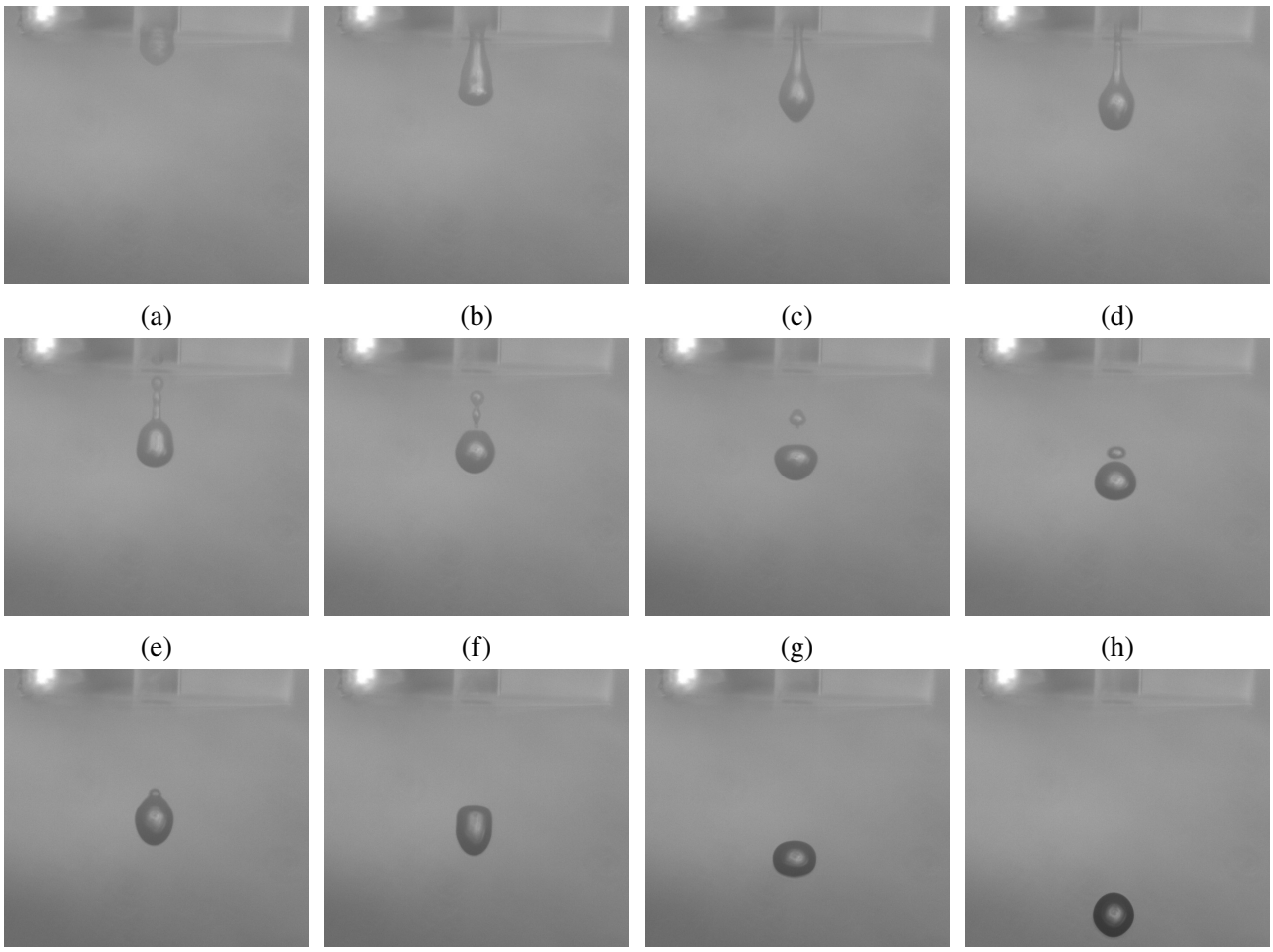

Figure 5.3: Image sequence of droplet formation from a DOD system. Liquid is pushed out of the nozzle and forms a column (a – b), which deforms due to the difference in fluid velocity between the nozzle exit and column head (c). Decrease of the column radius causes the pinch – off of the head and tail of the droplet, at the nozzle exit (d – e). The tail breaks up into satellite droplets due to Plateau-Rayleigh instabilities or 'pinch-off' from the main droplet (f – g). Satellite droplets merge with the main droplet (h – i), increasing its oscillation (j). The main droplet relaxes into a spherical shape (k – l).

the liquid column. At the nozzle exit, the liquid column's radius decreases until the liquid column detaches from the nozzle (Figures 5.3d and 5.3e). This process is referred to as the 'necking' of the liquid column, resulting in the 'pinch-off' of a liquid thread from the nozzle exit [27]. The thread head will form the main droplet, and the tail will either break up due to capillary waves or from pinch off from the main droplet (Figure 5.3f). Break up of the tail results in the formation of satellite droplets (Figure 5.3g), which can catch up and join the main droplet, depending on their velocity (Figures 5.3h and 5.3i). The merging of the satellite with the main droplet increasing the oscillation of the main droplet, which eventually relaxes into a spherical shape (Figures 5.3j to 5.3l).

Droplet diameter and velocity

Dijksman [28] developed an analysis of the hydrodynamics of small tubular pumps, to provide an approximation of the ejected droplet diameter and velocity. This analysis was used by Driessen and Jeurissen [29] to predict the droplet diameter d and velocity v_d in DOD systems, based on the conservation of momentum. The droplet volume V_d can be obtained by integrating the fluid flow $v(t)$ through the nozzle over time:

$$V_d = \int_{t_0}^{t_e} \pi r^2 v(t) dt, \tag{5.1}$$

where r is the radius of the liquid column. If we assume that the liquid column flowing through the nozzle has a radius equal to the nozzle's inner diameter, and that the liquid travels with a constant velocity v_j over a time $\delta t = t_e - t_0$. Here, δt corresponds to the time between initial emerging of liquid from the nozzle exit t_0, and the time t_e at which the jet velocity drops below the droplet velocity ($v_j < v_d$). The droplet volume is then given by

$$V_d = \delta t \pi r^2 v_j, \tag{5.2}$$

where r is the radius of the inner nozzle. Then we can obtain the droplet velocity, by considering the transferred momentum from the liquid column into the main droplet. The conservation of momentum includes three different terms: advection of the jet velocity, viscous tension, and surface tension. A combination of these three terms is used to approximate the droplet velocity:

$$v_d = \frac{1}{\rho V_d}\left(\delta t \rho \pi r^2 v_j^2 - 3\eta\pi r^2 - \delta t \pi r \gamma\right). \tag{5.3}$$

Here, the first terms corresponds to the advected momentum of jet velocity, the second term describes the decrease in momentum due to viscous tension and the third term considers the decrease in momentum due to the creation of new surface. After the droplet is ejected from the dispenser head, it will be decelerated to its terminal velocity v_t (derived in Section 2.2), which is given by

$$v_t = \frac{g d^2(\rho_d - \rho_a)}{6\eta_a}\left(1 + \frac{3}{16}Re\right)\frac{1+\kappa}{3\kappa+2}. \tag{5.4}$$

5.2 Experimental setup

The DOD system in our experimental setup is produced by Microdrop Technologies, the system consists of a dispenser head, liquid reservoir and an electronic pulse generator. The dispenser head (MD-K-130) has an inner nozzle diameter of 70 μm, and is suited for producing microdroplets up to 100 μm. The pulse generator, also produced by Microdrop Technologies, is used to provide the pulsed waveform. For a single peak waveform, three settings can be adjusted: pulse voltage, pulse width, and pulse frequency. The pulse frequency sets the time in between each contraction of the piezo actuator, adjusting the period between waveforms, which determines the dispensing frequency. The pulse voltage can be adjusted within a range of -250 to 250 V, the pulse width has an adjustable range of 1 to 200 μs, and the pulse frequency f has an adjustable range of 1 to 6000 Hz.

For our experiment, three different liquids are used to determine the influence of liquid properties on droplet diameter and velocity: distilled water, ethanol and ethylene glycol. Table 5.1 shows the liquid properties of the three liquids, which include density, surface tension, dynamic viscosity, vapor pressure, and acoustic wave velocity. Ethanol is selected because of its significantly lower density/surface tension ratio, and ethylene glycol for its possible suitability for vacuum systems. A different density/surface tension ratio influences the Weber number, and as a result the droplet dynamics. For future studies, the microdroplet setup is envisioned to operate in a non-atmospheric environment. In these low pressure environments, distilled water freezes within a few milliseconds [30]. Ethylene glycol has a lower vapor pressure and freezing temperature, which allow microdroplets of ethylene glycol to survive for up to 50 seconds without freezing [31].

For visualization, a camera and pulsed LED diode are placed at opposite ends of the droplet stream. The pulsed LED diode creates light flashes to illuminated the droplet for a short period of time, such that the pulse width of the diode sets the exposure time of the imaging system. The diode is also produced by Microdrop Technologies, and can be driven by the same waveform generator as the dispenser head. In this way, the timing of the droplet generation and flash light from the diode is automatically synchronized. The diode signal can be delayed with respect to the dispenserhead signal, by setting the delay time of the diode signal, which can be set within a range of 1-1000 μs. The setting menu for adjusting the pulse voltage, pulse width and pulse frequency is shown in Figure 5.4a. To avoid an overlay of multiple droplets, the camera's exposure time is limited by $\frac{1}{f}$.

The last part of the experimental setup is the micrometer sized pillar, the complete setup is shown in Figure 5.4b. The pillar is treated with a hydrophobic surface coating, to avoid spreading of the droplet on the pillar surface. Mechanical manipulators are used to move all the different parts of the experimental setup, in order to achieve correct alignment. The correct alignment of droplet stream and camera is achieved by first adjusting the camera position, until a sharp image of the nozzle tip is obtained. Due to the small depth of field of the imaging system, a sharp image of the dispenser head

liquid properties	distilled water	ethanol	ethylene glycol
density (kg/m^3)	998	789	1113
surface tension (mN/m)	72.8	22.3	47.7
dynamic viscosity (mPa $\cdot$ s)	1.1	1.2	19.8
vapor pressure (mbar)	23	60	$67 \cdot 10^{-3}$
acoustic wave velocity (m/s)	1482	1159	1660

Table 5.1: Liquid properties of distilled water, ethanol and ethylene glycol.

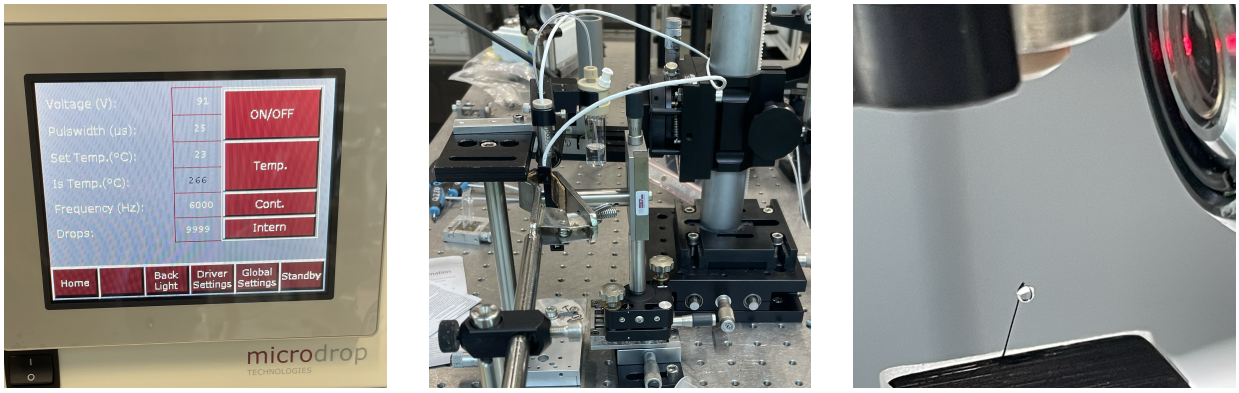

(a) (b) (c)

Figure 5.4: Pictures of the microdroplet setup: the main menu of the Microdrop Technologies pulse generator (a), alignment of the microdroplet generator with the imaging system (b), and close up of the pillar (c).

does not automatically give a sharp image of the droplet. Therefore, the camera position is adjusted further to find a sharp image of the droplet stream. Alignment of the pillar with the droplet stream can then be achieved, by adjusting the pillar position until a sharp image of the pillar is found. The magnification of the imaging system is obtained by using a calibration target (Thorlabs R1L3S5P). This target contains several 1 by 1 mm squares with variable amount of line pairs per mm (lp/mm). The distance between the first and last line pair of a 10 lp/mm square is determined to calculate the pixel size. The camera lens only has one configuration, so only one calibration is needed; the pixel size is 0.953 μm/pixel.

Threshold for image analysis

The pillar, which is initially introduced in the setup for droplet impact, will also be used to determine the threshold for our image analysis. First, the pillar diameter is measured, by using a similar approach as for the determination of droplet diameters in Chapter 4, a detailed description of the diameter measurement is given in Appendix B. The pillar diameter is found to be 100.75 ± 0.25 μm. Then, the pillar is placed in the same plane as the droplet stream, to capture images with exactly the same light conditions as for the droplet stream. Then these images are averaged and analyzed to obtain pillar sizes at different threshold values. The pillar diameter as a function of threshold values is shown in Figure 5.5 (purple line), where the dashed line indicates the measured pillar diameter (100.75 μm) . Intersection of the two lines is found at a threshold value of 29 %, which will be used as our threshold value for image analysis.

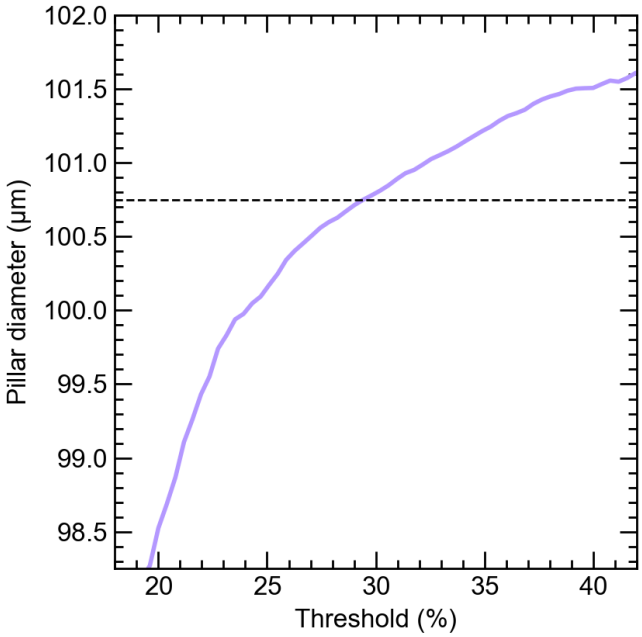

Figure 5.5: Plot of the pillar diameter as a function of threshold values. The actual pillar diameter is measured, and found to be 100.75 µm, which is indicated by the dashed line. The intersection of the two diameter values is found at a threshold value of 29 %.

5.3 Results

For all three liquids, the droplet diameter and velocity was determined for a range of pulse voltages and pulse widths. For each liquid, measurements were taken at 5 different time delays. Approximately 1000 images were taken at each time delay, to increase the accuracy of the mean diameter and center position for each data point. The droplet diameter was obtained from an average over 5 different time delays, to minimize the influence of droplet shape, inconsistent background light, and camera alignment. The droplet velocity was obtained by applying a linear fit to the average center position at each time delay. For DI water, measurements were taken over a range of time delays from 500 to 800 µs, and for ethanol and ethylene glycol at a range of time delays from 400 to 900 µs. These were chosen to ensure maximum distance between the droplet position at each time delay, to reduce the influence of position uncertainty on the droplet velocity.

Droplet diameter

The obtained values for droplet diameter at different pulse voltages, for distilled water and ethanol, are plotted on the left side of Figure 5.6. The range of pulse voltages is limited by the stability of the dispensed droplet stream, in the range of -96 to -100 V the droplet stream was stable for both distilled water and ethanol. For both liquids an increase in pulse voltage results in an increase in droplet diameter. The pulse voltage directly influences the magnitude of the induced pressure wave, and an increased pressure wave increases the ejected droplet volume [32]. The increase in droplet diameter for increased pulse voltage is in agreement with prior research [33].

On the right side of Figure 5.6, the obtained values for droplet diameter of ethylene glycol are given, for a range of -152 to -160 V. The required pulse voltage for droplet formation is higher for ethylene glycol, due to the higher viscosity of ethylene glycol (19.8 mPa · s) compared to distilled

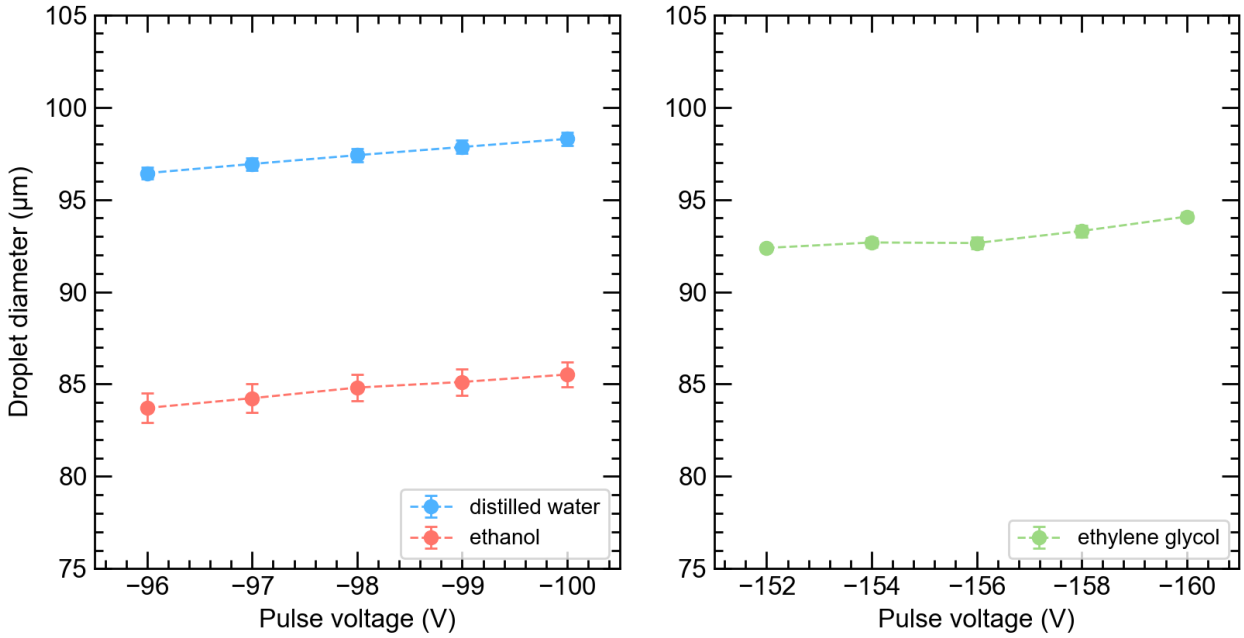

Figure 5.6: Results for droplet diameters as a function of pulse voltage. The left plot shows the mean droplet diameters for distilled water (●) and ethanol (●), measured in a range of pulse voltage from -96 to -100 V. The right plot shows the mean droplet diameters for ethylene glycol (●), measured in a range of pulse voltage from -152 to -160 V. For all three liquids the pulse width was set at 45 µs, and the pulse frequency at 15 Hz.

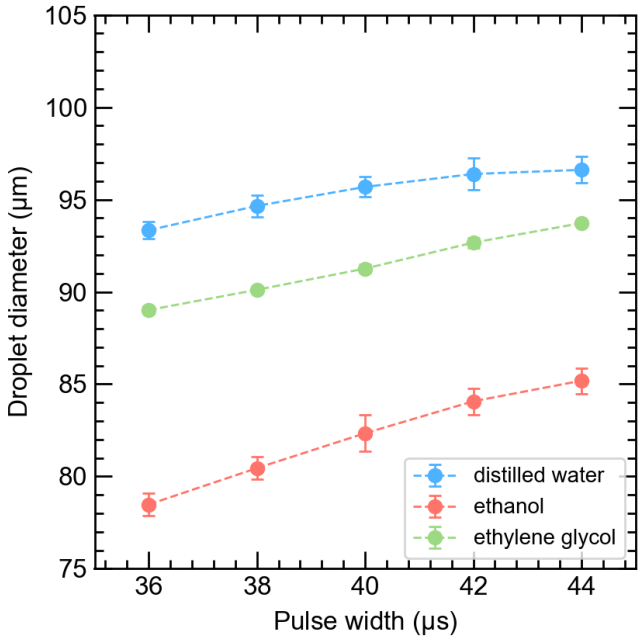

Figure 5.7: Results for droplet diameters as a function of pulse width, for distilled water (●) , ethanol (●) and ethylene glycol (●). All three liquids were measured in a range of 36 to 44 µs, and with pulse frequency set to 15 Hz. For distilled water and ethanol, the pulse voltage was set at -100 V, and for ethylene glycol at -160 V.

water and ethanol (1.1 – 1.2 mPa · s). The liquid viscosity influences the droplet formation process in three different ways. First, viscous dissipation reduces the magnitude of the induced pressure wave arriving at the nozzle exit, resulting in a lower jet velocity [34, 32] . Then, a higher viscosity increases the resistance of the fluid flow through the nozzle, decreasing the ejected liquid volume [35]. Finally, when a droplet is formed from the liquid column, Equation 5.3 indicates that a higher viscosity results in a lower droplet velocity. Therefore, a higher pulse voltage was required to achieve the formation of droplets for ethylene glycol, which is also in agreement with prior research [33]. For investigating the influence of fluid properties on droplet formation in DOD system, Fromm [36] introduced the Z number, the inverse of the Ohnesorge number (Equation 2.6):

$$Z = Oh^{-1} = \frac{Re}{\sqrt{We}} = \frac{\sqrt{\rho\sigma d}}{\eta}. \tag{5.5}$$

A previous study has shown that around Z = 10, viscous dissipation starts to significantly influence the required pulse voltage needed to operate the microdroplet generator, which is in line with our findings [33].

For the droplet diameter as a function of pulse width, all three liquids were measured within a range of 36 to 44 µs. Although for all three liquids the droplet diameter increases for increasing pulse width, there is a significant difference between the absolute increase. For distilled water, the droplet diameter increases by ~3 µm, whereas for ethylene glycol the droplet diameter increases by ~5 µm, and for ethanol by ~7 µm. The pulse width influences the overlap of the two pressure waves traveling through liquid in the dispenser head capillary. In theory, when the pulse width is equal to l/c, the overlap of the two waves is optimal, leading to the highest positive pressure wave arriving at the nozzle. The increase in droplet volume for increasing pulse width indicates that the optimal value was not within the examined range. The optimum pulse width is influenced by the acoustic wave velocity, which explains the difference in absolute increase of the droplet diameter for the three different liquids.

Droplet velocity

The influence of pulse voltage on droplet velocity, for a range of -96 to -100 V, is shown in the middle panel of Figure 5.8. For all measurements, the pulse width was set at 45 µs, and the pulse frequency at 15 Hz. The jet velocity was calculated from the results of droplet diameter and droplet velocity. For a simplified analysis, the jet velocity is assumed to be constant over the time δt, previous studies have shown this is a good approximation [33]. Using Equation 5.2 in equation Equation 5.3, and rearranging gives

$$v_j^2 - v_j v_d - \frac{3\eta}{\rho\delta t} - \frac{\gamma}{\rho r} = 0. \tag{5.6}$$

Equation 5.6 can be solved analytically to obtain v_j, considering only the solution where $v_j > v_d$:

$$v_j = \frac{1}{2}\left[v_d + \sqrt{v_d^2 + 4\left(\frac{3\eta}{\rho\delta t} + \frac{\gamma}{\rho r}\right)}\right] \tag{5.7}$$

To obtain the time δt, the droplet volume from Equation 5.2 is compared to the actual droplet volume, obtained from the experimental data. An optimization over different values for δt, for each pulse voltage, gives a mean value of δt which is used to determine the jet velocity. For water δt = 44.1 ± 0.2 µs, for ethylene glycol δt = 47.1 ± 0.2 µs, and for ethanol δt = 49.0 ± 0.3 µs. The difference in δt between the three liquids is unexpected, since a previous study in which different liquids were

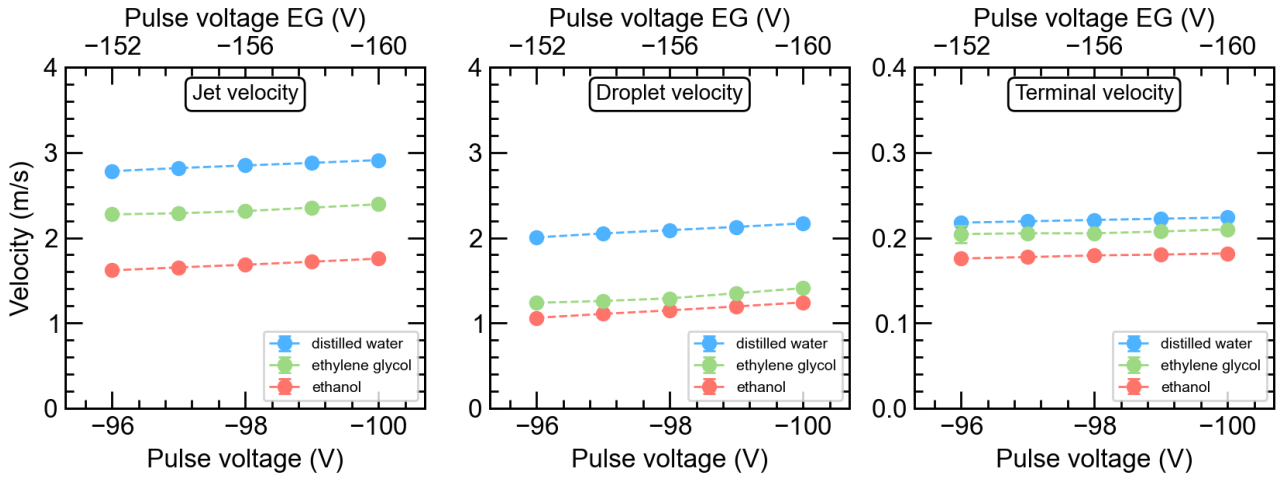

Figure 5.8: Results for three types of velocities as a function of pulse voltage: jet velocity, droplet velocity and terminal velocity. The jet velocity is calculated from Equation 5.6, where δt is estimated by comparing the droplet volume from Equation 5.2 to the experimental data. The terminal velocity is calculated from Equation 5.4. Note the difference in scaling between the left/middle panels and the right panel. The initial droplet velocity is almost a factor of 10 times higher than the terminal velocity. For all plots, the top x-axis represents the pulse voltages for ethylene glycol (-152 to -160 V), and the bottom x-axis represents the pulse voltages for distilled water and ethanol. All measurements were taken at a pulse width of 45 µs and frequency of 15 Hz.

examined argued that for all liquids the same value for δt can be used [33]. The measured difference in δt is attributed to the operation mode of the DOD system in our experiment, where a negative pulse voltage is applied. The propagation of pressure waves depends on the acoustic wave velocity (see Table 5.1), which differs per liquid. The difference in wave velocity results in a different overlap of pressure waves, even though the applied pulse width is the same. As a result, the distribution of the pressure wave arriving at the nozzle will be different for all three liquids, resulting in a different jetting velocity and δt. The influence of viscosity on droplet velocity can be clearly seen when comparing the jet/droplet velocity of water and ethylene glycol: jet velocities lie closer together than droplet velocities. During the pinch-off process, the liquid thread is pulled back into the nozzle, slowing down the main droplet. As predicted by Equation 5.3, droplet velocity is reduced by the increased viscosity of ethylene glycol. The right panel of Figure 5.8 shows the terminal velocity predicted by Equation 5.4. Note the difference in scaling between the left/middle panel and the right panel; the terminal velocity is much lower than the initial droplet velocity. Since the terminal velocity scales with the droplet diameter as $v \sim d^2$, the influence of voltage on terminal velocity is negliaible. The difference in terminal velocities for the three liquids is explained by the difference in droplet diameter: for water d = 96 – 99 µm, for ethylene glycol d = 92 – 95 µm and for ethanol d = 83 – 86 µm.

The influence of pulse width on the droplet velocity was investigated in a similar manner. Measurements were taken in a range of 36 to 44 µs, for all three liquids. For distilled water and ethanol, the pulse voltage was set at -100 V, and for ethylene glycol the pulse voltage was set at -160 V. For all three liquids the pulse frequency was set at 15 Hz. The left plot in Figure 5.9 shows the calculated jet velocity, which is obtained in a similar manner as was done for the pulse voltage. However, since the change in pulse width results in a change in pressure wave overlap and duration of the induced pressure wave, the value for δt differs for each data point. The middle panel of Figure 5.9 shows the droplet velocity, which seems to be slightly more affected by changes in pulse width, compared to

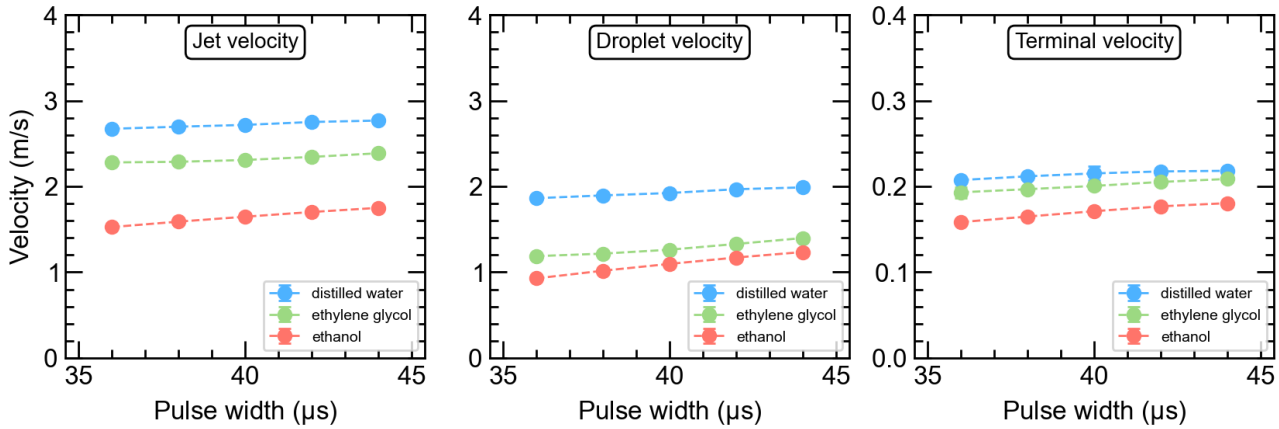

Figure 5.9: Results for three types of velocities as a function of pulse width: jet velocity, droplet velocity and terminal velocity. The jet velocity is calculated from Equation 5.6, where δt is estimated by comparing the droplet volume from Equation 5.2 to the experimental data. The terminal velocity is calculated from Equation 5.4. Note the difference in scaling between the left/middle panels and the right panel. The initial droplet velocity is almost a factor of 10 times higher than the terminal velocity. For distilled water and ethanol, measurements were taken at a pulse voltage of -100 V. For ethylene glycol, the pulse voltage was set at -160 V. All measurements were taken at a pulse width of 45 µs, and a frequency of 15 Hz.

the change in pulse voltage. The droplet velocity shows a slightly different trend for each liquid, a result of the difference in acoustic wave velocity. There is a minimal increase in terminal velocity for increasing pulse width; a result of the increase in droplet diameter for increasing pulse width.

Microdroplet impact on similar sized pillar

Our imaging system was used to create an image sequence of the microdroplet impact on a similar sized pillar ($\approx$ 100 µm). The image sequence is shown in Figure 5.10, where the images are taken at increasing delay times. When the initial spherical droplet (Figure 5.10a) impacts the pillar, the droplet diameter increases (Figures 5.10b to 5.10d). The droplet impact is not strong enough to overcome the droplet surface tension, which is indicated by a low weber number: We $\approx$ 4. Instead of continuously increasing, the droplet diameter decreases (Figures 5.10e to 5.10h), and increases again (Figures 5.10i and 5.10j). The oscillation of the droplet diameter has been observed in previous studies of microdroplet impact on a solid surface [37]. The hydrophobic coating on the pillar normally prevents the droplet from spreading. However, droplets which do not break up accumulate on the pillar surface and eventually form a big droplet, which stays attached to the pillar. In this way, droplets impacting the pillar are affected by the droplets that came before them. The whitish glow on the left side of each image in Figure 5.10 is a result of light reflecting from a 'big' droplet attached to the micro pillar (see Figure 5.4c).

To achieve a droplet deformation that shows sheet formation, the Weber number of the droplet impact has to be increased. To obtain a larger Weber number for a similar droplet diameter, we need to increase either the droplet velocity or the ratio of surface tension to density. A similar droplet velocity for ethanol would result in a factor 3 increase in Weber number. Since the optimum pulse width for ethanol was not achieved in the examined range, it could be possible to (at least) achieve similar droplet velocity for ethanol as for water by finding the optimal pulse width. As the Weber number scales with velocity, like $We \sim v^2$, increasing the velocity is the most efficient way to achieve sheet formation.

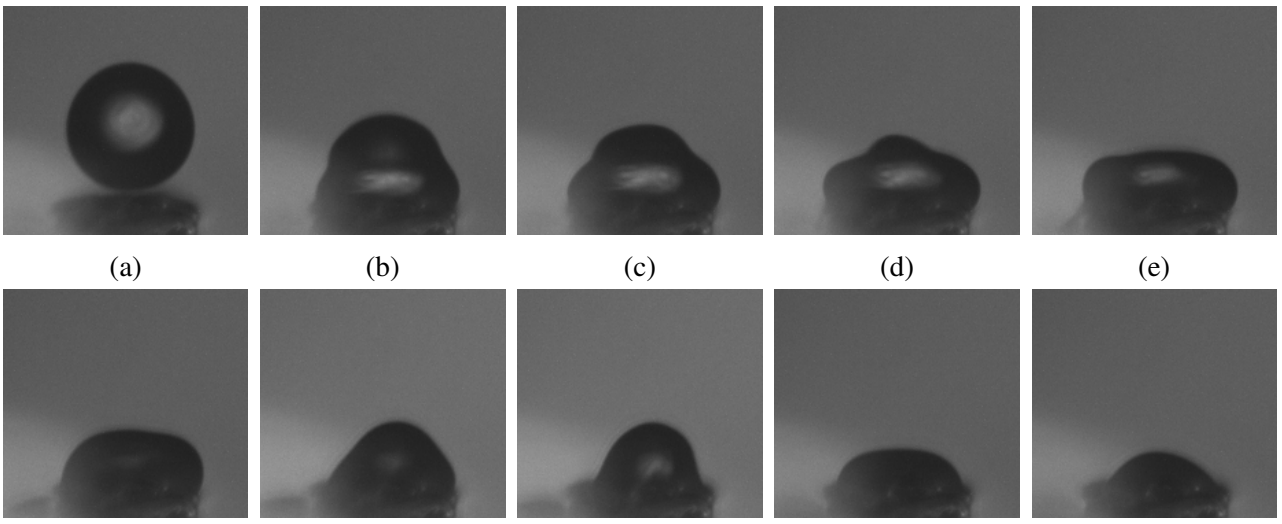

Figure 5.10: Impact of microdroplets on a similar sized pillar. The stroboscopic image sequence shows the oscillation of the droplet diameter after impact. The droplet does not break up due to the relative strong surface force, compared to the inertial force. This is indicated by the low Weber number of the impact: We $\approx$ 4.

5.4 Conclusions

We developed a setup to visualize microdroplet impact on a similar sized pillar. Microdroplet are generated by using a droplet-on-demand system, operated in negative pulse voltage mode. The influence of liquid properties,pulse voltage, and pulse width on droplet diameter and velocity was investigated. For distilled water, droplet diameters in a range of 96 – 99 μm were found for pulse voltages of -96 and -100 V, and pulse widths of 36 to 45 μs. For ethanol, droplet diameters in a range of 83 – 86 μm were found for pulse voltages and pulse widths in the same range. The difference in droplet diameter and velocity can be explained by the difference in acoustic wave velocity. For ethylene glycol, droplet diameters in a range of 92 – 95 μm were found, but a higher pulse voltage (-160 V) was required to achieve stable droplet formation, due to the viscous dissipation of pressure waves inside the glass capillary.

The highest droplet velocity was achieved for water where v_d = 1.9 – 2.2 m/s. Ethanol and ethylene glycol showed a similar droplet velocity, for which v_d = 0.9 – 1.2 m/s and v_d = 1.2 – 1.4 m/s respectively. Although the jet velocity for ethylene glycol was higher than for ethanol, the decrease in droplet velocity due to increased viscosity resulted in a similar droplet velocity for both liquids. For all three liquids, the increase in droplet diameter/velocity for increasing pulse width indicated that the optimum pulse width was not found within the examined range.

An image sequence of the droplet oscillation after pillar impact shows our setup was successful in visualization of droplet dynamics at micro scale. Due to the low Weber number (We $\approx$ 4), the droplet showed diameter oscillations instead of continuously increasing diameter. Unlike for the case of higher Weber numbers, no sheet formation was observed. The visualization of the droplet impact provided some challenges, mainly resulting from the accumulation of droplets on the pillar tip. To visualize sheet formation, the droplet velocity has to be increased.

5.5 Outlook

For visualization of sheet formation with our current setup the droplet velocity must be higher, without changing the current droplet size. The results for ethanol indicated that an optimum pulse width was not yet reached, being able to operate the microdroplet generator at the optimal pulse width is likely to increase the droplet velocity. If similar velocities for ethanol can be achieved as for water, the Weber number will increase by a factor of 3. A three times larger Weber number could be sufficient to show different droplet deformation, because it is likely to prevent droplet accumulation on the pillar tip. Visualization of droplet dynamics at these slightly larger Weber numbers would be a next step for the setup. However, for future fluid dynamic studies of laser-droplet interactions, the microdroplet setup will have to be placed in a non-atmospheric environment. To ensure the microdroplet generator can be operated at low pressures, ethylene glycol was already tested and proved usable. In addition, a vacuum chamber is assembled to do some initial tests on the operation of the microdroplet generator in vacuum. Figure 5.11 shows the vacuum chamber, and the camera with long-distance microscope. First short tests have shown that no boiling appears down to a pressure of 20 mbar, indicating running the microdroplet generator is possible at pressures of 1000 – 20 mbar. Additional (longer) tests with constant low pressures are required to confirm this.

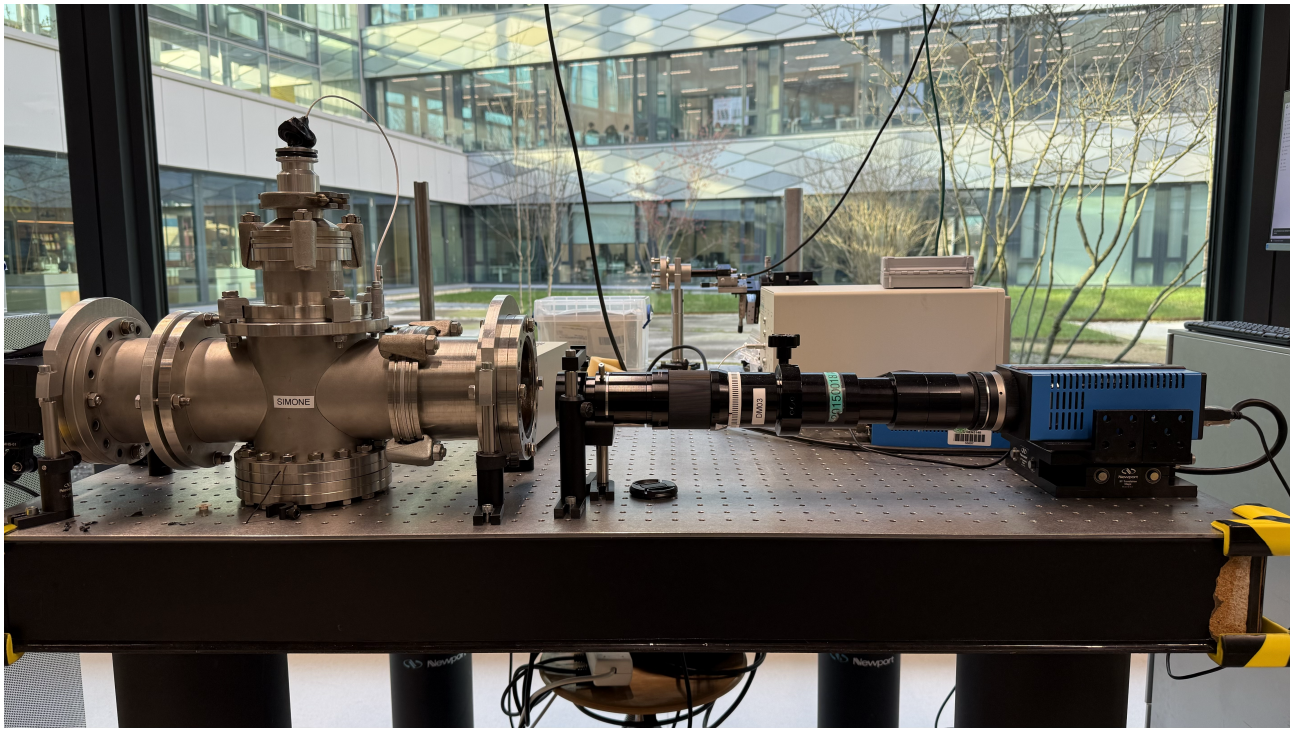

Figure 5.11: A new setup is developed/implemented to operate the microdroplet generator in a non-atmospheric environment. The camera (PCO-4000) is equipped with a long distance microscope (K2 DistaMax), with a working distance of 228 – 388 mm. First tests have shown that a pressure of 20 mbar can be achieved.

Chapter 6

Conclusion

We have developed two experimental setups, to visualize droplet dynamics at millimeter and micrometer scale. The development of the millimeter setup was used to gain experience with imaging techniques, trigger systems and image analysis. Image sequences ("movies") of droplet deformation after pillar impact showed that the development of our imaging system was successful. Characterization results of the millimeter setup provided a Weber number range of 50 – 550, where the upper limit is mainly determined by the droplet's falling height. The insights from the millimeter setup provided a starting point for the development of the second setup at micrometer scale.

For the micrometer setup, a DOD system was used to generate a microdroplet stream, which can be aligned with a micrometer sized pillar. We investigated the influence of different liquid properties and generator settings on droplet diameter and velocity. Three different liquids were examined, which turned out all to be suitable for stable droplet formation. Acoustic wave theory predicts a different pressure wave overlap for the three liquids, with accompanying difference in jet velocity at the nozzle exit. This was confirmed by our experimental results, where the largest droplet diameter and highest velocity were found for water. Ethylene glycol droplets have a slightly smaller diameter compared to water, but significantly lower droplet velocity. The decrease in droplet velocity is a result of the increased viscosity of ethylene glycol, which also affected the range of operating pulse voltages. For ethanol, the significantly smaller droplet diameter and lower velocity indicated our range of examined pulse widths did not include the optimal pulse width. We provided an image sequence of the droplet deformation after pillar impact on micro scale, confirming the successful development of our imaging system. The accumulation of droplets on the pillar tip provided some challenges for visualization of the droplet deformation. This problem can be solved by increasing the Weber number, which can be achieved by operating the microdroplet generator at the optimum pulse width, or by operating it in a vacuum environment; in both cases the increased velocity leads to a higher Weber number. First tests have been performed to confirm the suitability of the microdroplet generator in a vacuum environment.

Bibliography

[1] D. Kurilovich, *Laser-induced dynamics of liquid tin microdroplets*. PhD thesis, Vrije Universiteit Amsterdam, 2019.

[2] D. Kurilovich, A. L. Klein, F. Torretti, A. Lassise, R. Hoekstra, W. Ubachs, H. Gelderblom, and O. O. Versolato, "Plasma propulsion of a metallic microdroplet and its deformation upon laser impact," *Physical review applied*, vol. 6, p. 014018, 2016.

[3] D. Kurilovich, M. M. Basko, D. A. Kim, F. Torretti, R. Schupp, J. C. Visschers, J. Scheers, R. Hoekstra, W. Ubachs, and O. O. Versolato, "Power-law scaling of plasma pressure on laser-ablated tin microdroplets," *Physics of Plasmas*, vol. 25, p. 012709, 2018.

[4] A. Mazumdar, "Principles and techniques of schlieren imaging systems," *Columbia University Computer Science Technical Reports*, vol. 14, 2013.

[5] A. L. Klein, W. Bouwhuis, C. W. Visser, H. Lhuissier, C. Sun, J. H. Snoeijer, E. Villermaux, D. Lohse, and H. Gelderblom, "Drop shaping by laser-pulse impact," *Physical review applied*, vol. 3, p. 044018, 2015.

[6] A. L. Klein, D. Kurilovich, H. Lhuissier, O. O. Versolato, D. Lohse, E. Villermaux, and H. Gelderblom, "Drop fragmentation by laser-pulse impact," *Journal of fluid mechanics*, vol. 893, p. A7, 2020.

[7] Y. Wang and L. Bourouiba, "Drop impact on small surfaces: thickness and velocity profiles of the expanding sheet in the air," *Journal of Fluid Mechanics*, vol. 814, pp. 510–534, 2017.

[8] R. Gunn and G. D. Kinzer, "The terminal velocity of fall for water droplets in stagnant air," *Journal of the Atmospheric Sciences*, vol. 6, pp. 243–248, 1949.

[9] P. K. Kundu, I. M. Cohen, D. R. Dowling, and J. Capecelatro, *Fluid mechanics*. Elsevier, 2024.

[10] A. I. Ruban and J. S. Gajjar, *Fluid Dynamics: Classical Fluid Dynamics*. Oxford University Press, 2014.

[11] E. Villermaux and B. Bossa, "Drop fragmentation on impact," *Journal of Fluid Mechanics*, vol. 668, pp. 412–435, 2011.

[12] K. Beard and H. Pruppacher, "A determination of the terminal velocity and drag of small water drops by means of a wind tunnel," *Journal of the Atmospheric Sciences*, vol. 26, pp. 1066–1072, 1969.

[13] G. B. Foote and P. Du Toit, "Terminal velocity of raindrops aloft," *Journal of Applied Meteorology*, pp. 249–253, 1969.

[14] J. Hadamard, "Slow permanent movement of a viscous liquid sphere in a viscous liquid," *CR Acad. Sci.*, vol. 152, pp. 1735–1738, 1911.

[15] B. F. Edwards, J. W. Wilder, and E. E. Scime, "Dynamics of falling raindrops," *European Journal of Physics*, vol. 22, p. 113, 2001.

[16] J. H. Van Boxel *et al.*, "Numerical model for the fall speed of rain drops in a rain fall simulator," in *Workshop on wind and water erosion*, vol. 5, pp. 77–85, 1997.

[17] M. Versluis, "High-speed imaging in fluids," *Experiments in fluids*, vol. 54, pp. 1–35, 2013.

[18] G. Bradski, "The OpenCV Library," *Dr. Dobb's Journal of Software Tools*, 2000.

[19] H. Yuen, J. Princen, J. Illingworth, and J. Kittler, "Comparative study of hough transform methods for circle finding," *Image and vision computing*, vol. 8, pp. 71–77, 1990.

[20] Z. Wang, Y. Zhang, R. Li, Q. Wang, and J. Wang, "An experimental study on drop formation from a capillary tube," *Journal of the Brazilian Society of Mechanical Sciences and Engineering*, vol. 42, pp. 1–13, 2020.

[21] W. D. Harkins and F. Brown, "The determination of surface tension (free surface energy), and the weight of falling drops: The surface tension of water and benzene by the capillary height method.," *Journal of the American Chemical Society*, vol. 41, pp. 499–524, 1919.

[22] G. F. Scheele and B. J. Meister, "Drop formation at low velocities in liquid-liquid systems: Part i. prediction of drop volume," *Aiche journal*, vol. 14, pp. 9–15, 1968.

[23] X. Zhang and O. A. Basaran, "An experimental study of dynamics of drop formation," *Physics of fluids*, vol. 7, pp. 1184–1203, 1995.

[24] A. L. Klein, *Laser impact on flying drops*. PhD thesis, University of Twente, 2017.

[25] C.-K. Yu, P.-R. Hsieh, S. E. Yuter, L.-W. Cheng, C.-L. Tsai, C.-Y. Lin, and Y. Chen, "Measuring droplet fall speed with a high-speed camera: indoor accuracy and potential outdoor applications," *Atmospheric Measurement Techniques*, vol. 9, pp. 1755–1766, 2016.

[26] D. B. Bogy and F. Talke, "Experimental and theoretical study of wave propagation phenomena in drop-on-demand ink jet devices," *IBM Journal of research and development*, vol. 28, pp. 314–321, 1984.

[27] H. Dong, W. W. Carr, and J. F. Morris, "An experimental study of drop-on-demand drop formation," *Physics of fluids*, vol. 18, p. 072102, 2006.

[28] J. Dijksman, "Hydrodynamics of small tubular pumps," *Journal of Fluid Mechanics*, vol. 139, pp. 173–191, 1984.

[29] T. Driessen and R. Jeurissen, "Drop formation in inkjet printing," *Fundamentals of Inkjet Printing: The Science of Inkjet and Droplets*, pp. 93–116, 2016.

[30] K. Ando, M. Arakawa, and A. Terasaki, "Freezing of micrometer-sized liquid droplets of pure water evaporatively cooled in a vacuum," *Physical Chemistry Chemical Physics*, vol. 20, pp. 28435–28444, 2018.

[31] K. Ando, M. Arakawa, and A. Terasaki, "Evaporation processes of a liquid droplet of ethylene glycol in a vacuum," *Chemistry Letters*, vol. 45, pp. 961–963, 2016.

[32] H.-C. Wu and H.-J. Lin, "Effects of actuating pressure waveforms on the droplet behavior in a piezoelectric inkjet," *Materials transactions*, vol. 51, pp. 2269–2276, 2010.

[33] Y. Liu and B. Derby, "Experimental study of the parameters for stable drop-on-demand inkjet performance," *Physics of Fluids*, vol. 31, p. 032004, 2019.

[34] N. Reis, C. Ainsley, and B. Derby, "Ink-jet delivery of particle suspensions by piezoelectric droplet ejectors," *Journal of Applied Physics*, vol. 97, p. 094903, 2005.

[35] H.-C. Wu, W.-S. Hwang, and H.-J. Lin, "Development of a three-dimensional simulation system for micro-inkjet and its experimental verification," *Materials Science and Engineering: A*, vol. 373, pp. 268–278, 2004.

[36] J. Fromm, "Numerical calculation of the fluid dynamics of drop-on-demand jets," *IBM Journal of Research and Development*, vol. 28, pp. 322–333, 1984.

[37] H. Dong, W. W. Carr, and J. F. Morris, "Visualization of drop-on-demand inkjet: Drop formation and deposition," *Review of Scientific Instruments*, vol. 77, p. 085101, 2006.

Acknowledgments

None of the work I've written about would have been possible without the help and guidance of others, and I would like to thank the people who contributed to this project. First of all, thank you Ronnie for providing me with the opportunity to do this project, for arranging a 65 ECTS master project, for all your non-ion related knowledge and giving me the freedom to learn and develop myself. I'm especially grateful for your willingness and flexibility to let me combine my academic career with a high level sports career, now and in the near future. Also, I would like to thank Oscar for being the second examiner, and for the guidance and feedback on all fluid dynamics related stuff.

Thanks to all the PhD's/postdocs of the Ion interactions group: Emiel, Lennart, Luc and Klaas, for providing a welcoming and supportive environment. Especially thanks to Luc, for all of your help, guidance and honest feedback. Also thanks to Mart, for the technical support, I still wonder if there is anything in the lab you actually can't fix. All of you made this somewhat difficult year in Groningen very enjoyable, and I look forward to working together with most of you for the next four years. Finally, I would like to thank the people from the DALEK 2 group at ARCNL, for providing me with input on all fluid dynamic related aspects of my project. Especially to Dion, for your explanation of the data analysis codes and input on imaging methods. Working together with all the people form both ARCNL and the QISD group has thought me a lot, both in terms of academics and general life lessons.

Appendices

A Pillar diameter

The pillar diameter was measured by using a similar method to the one described in Chapter 4. First, we take a shadowgraph image of the pillar, which can be seen in Figure 1. The intensity of the light source is set to ensure a uniform white background. The image of the pillar is not uniformly sharp (due to some bending of the pillar), such that only the highlighted area is used for our diameter measurement. The average gradient value for each threshold value is determined; a total of 1000 images are analyzed. The plot of the average gradient as a function of threshold is shown in Figure 2. A maximum for the average gradient is found at a threshold of 47%. The threshold value is used to determine the pillar area in Figure 1, which can be approximated by the area of a parallelogram: area = base x height. Determining the base from Figure 1, introduces an uncertainty in the pillar diameter, as a result of the resolution of the imaging system (R_s = 0.953 μm). The pillar diameter is found to be 100.75 ± 0.25 μm.

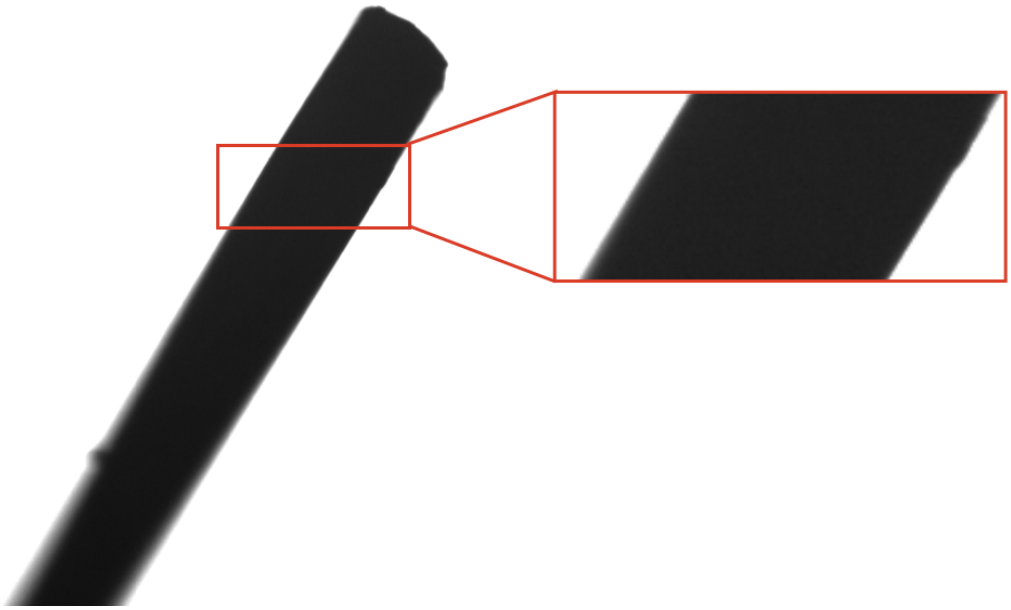

Figure 1: Shadowgraph image of the pillar, where the highlighted area indicates the region which is used for size measurement.

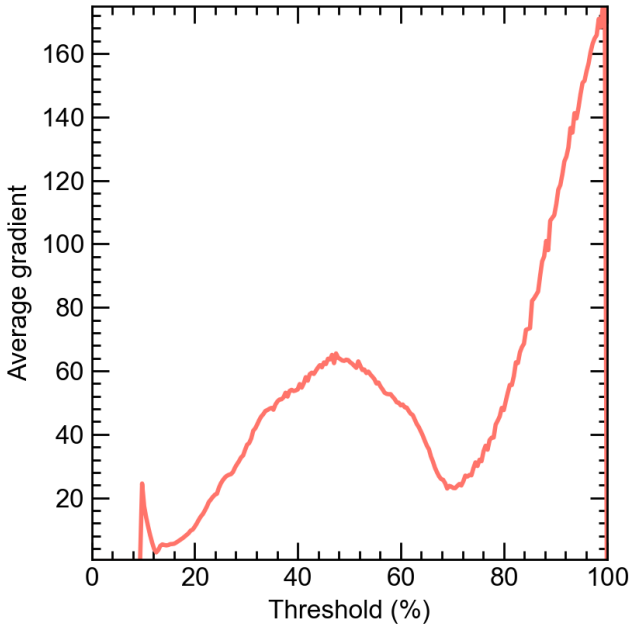

Figure 2: Average gradient as a function of threshold value, for the pillar image in Figure 1. The peak of the average gradient value is located at a threshold of 47%.